TUD-L2B-EWH_UNC-GRACE: A GLOBAL LEVEL-2B GRACE(-FO) EWH UNCERTAINTY PRODUCT

A PREPRINT

Michal Cuadrat-Grzybowski*
Space Engineering Department
Delft University of Technology
Kluyverweg 1, 2629 HS Delft (the) Netherlands
M.Cuadrat-Grzybowski-1@tudelft.nl

Joao G. Teixeira da Encarnacao
Space Engineering Department
Delft University of Technology
Kluyverweg 1, 2629 HS Delft (the) Netherlands
j.g.deteixeiradaencarnacao@tudelft.nl

May 8, 2026

ABSTRACT

We present a globally gridded Level-2B GRACE(-FO) equivalent water height (EWH) data product that provides a complete characterisation of uncertainty, enabling easy direct use in Earth system research. Unlike conventional uncertainty estimates that either require propagation of full normal matrices or rely on empirical assumptions about temporal and spatial correlations, TUD-L2B-EWH_UNC-GRACE combines ensemble statistics from multiple independently processed Level-2 solutions to quantify uncertainties, including contributions from ocean tide model differences, parametrization strategies, and uncertainties in the Atmosphere and Ocean De-aliasing product. Post-processing uncertainties, related to filtering effects and Glacial Isostatic Adjustment (GIA) model variability, are quantified using a known-pair approach and an ensemble of 56 GIA models, respectively. Uncertainty fields are provided for a suite of anisotropic filtering strategies (DDK2–DDK7), supporting the assessment of filtering strength, leakage effects, and processing-choice impacts on total uncertainty. In addition to the standard Level-2B configuration, the ancillary TUD-L2B-EWH_UNC_noSLR-GRACE product, in which low-degree coefficients ($C_{2,0}$ and $C_{3,0}$) are not replaced by Satellite Laser Ranging estimates, allows users to isolate uncertainties associated with low-degree coefficient treatment. TUD-L2B-EWH_UNC is the first Level-2B EWH dataset to deliver end-to-end, gridded uncertainty fields, to facilitate robust applications in hydrology, glaciology, solid-Earth, and oceanographic studies. Ancillary tidal corrections and climatological fits, for long-term climatological studies, are distributed separately in the TUD-L2B-EWH_CLIM-GRACE, TUD-L2B-EWH_CLIM_CORR-GRACE and TUD-L2B-EWH_CLIM_LEAKAGE-GRACE products.

Keywords GRACE, Uncertainty, Global, Level-2B, Gravimetry, geophysics.

1 Introduction

The Gravity Recovery and Climate Experiment (GRACE) and its successor GRACE-FO (GFO) [Tapley et al., 2004, Landerer et al., 2020] provide continuous observations of Earth's time-variable gravity field, enabling direct monitoring of mass redistribution and equivalent water height (EWH) variations. The mission data are organised into several processing levels. Level-1(A/B) contains raw and calibrated satellite measurements respectively, including inter-satellite range and range rate from the microwave system, accelerometer observations, GPS orbits, and attitude data [Case et al., 2010]. Level-2 comprises monthly spherical harmonic coefficients (SHCs) that represent the gravity field recovered by numerous processing centres. At this stage, the solutions reflect the outcome of the gravity inversion but do not yet include standard post-processing steps such as mean field removal, filtering, geocentre restoration, replacement of low-degree coefficients, or mitigation of tidal aliasing.

*Corresponding author.

Level-2B provides the next processing stage, in which SHCs are synthesised into gridded EWH fields and converted into anomalies by removing the long-term mean. Standard GRACE(-FO) post-processing is applied at this level [Dahle et al., 2025], including the addition of degree-1 geocentre motion [Swenson et al., 2008], replacement of $C_{2,0}$ and $C_{3,0}$ (GFO) [Loomis and Rachlin, 2023], glacial isostatic adjustment (GIA) correction, filtering, and mitigation of tidal aliasing (e.g., the 161-day S_2tide). As such, Level-2B delivers consistent and ready-to-use anomaly fields while remaining closer to the original spherical harmonic solutions, allowing users to apply their own spatial averaging and uncertainty treatments compared with higher-level products. Level-3 represents application-specific mass anomaly data, for example, ground or terrestrial water storage (GWS/TWS), ice-mass change, or ocean bottom pressure (OBP). These products extend Level-2B but require additional transformations, such as conversion from EWH to pressure units for ocean applications and even the re-addition of background model components such as GAA (non-tidal atmospheric component), GAB (oceanic component) or GAC (sum of the latter two components) [Dobslaw et al., 2018]. Within this hierarchy, Level-2B serves as a practical bridge between sets of SHC solutions (Level-2) and analysis-ready Level-3 products, facilitating researchers to customise filtering and corrections for hydrology, glaciology, solid-Earth, or oceanographic studies.

Despite the extensive use of these datasets, uncertainty quantification remains a major challenge, particularly in assimilation frameworks that require independent observational error information [Velicogna et al., 2014, Blazquez et al., 2018, Yang et al., 2025, Wu et al., 2022, Retegui-Schiettekatte et al., 2025]. Full covariance matrices are generally not distributed with GRACE(-FO) Level-2 products (except for GFZ and ITSG), are difficult to reconstruct independently [Zhang et al., 2024], and often are unclear regarding the numerous and diverse underlying assumptions. Furthermore, gridded uncertainty fields suitable for end-user applications are largely unavailable, presenting an additional challenge for researchers to perform robust hydrological, glaciological, or solid-Earth analyses.

As a result, most practical uncertainty characterisations rely on approximate or empirically derived approaches [Boergens, 2021, Boergens et al., 2022]. For instance, the Global Gravity-based Groundwater Product (G3P) project [Güntner et al., 2024] adopts empirical models based on monthly GRACE(-FO) fields. Comparisons with uncertainties derived from full covariance propagation show that empirical estimates often overestimate absolute magnitudes, while their spatial correlations, when aggregated over major river basins, typically remain below 0.75 [Boergens et al., 2022]. Other statistical methods require collapsing either the temporal or spatial dimensions, thus reducing the information content of the original solutions [Chen et al., 2021, Gao et al., 2023]. For example, Chen et al. [2021] apply a three-cornered-hat (TCH) method to CSR, GFZ, and JPL SHC solutions, providing uncertainties resolved only in space, while Gao et al. [2023] extend this approach to mascon products using Bayesian fusion, which also yields spatially resolved uncertainties without capturing temporal variability. Although this yields a meaningful spatial representation of the error, the temporal component is effectively eliminated, and the reliance on three independent solutions introduces sensitivity to inter-center differences and filtering strategies. To address this, You et al. [2025] combine multiple GRACE monthly solutions in the spatial domain using several weighting strategies. In particular, they introduce an "oceanic accuracy" weighting scheme derived from residuals over the open ocean, which reduces noise and demonstrates that accounting for spatially varying signal-to-noise characteristics improves GRACE estimates of mass changes, which they validated over the Caspian Sea.

A further key element of the GRACE(-FO) error budget is uncertainty associated with GIA, a process essential when interpreting long-term variability in EWH, geoid, or other gravity-derived quantities. The ICE6G-D model [Peltier et al., 2018] is widely used, but more than 50 GIA models exist [Bagge et al., 2023], each with frequency-distinct signal characteristics. These differences can strongly influence geophysical trends, particularly in hydrology, and may even lead to contradictory interpretations of groundwater evolution [Caron et al., 2018, Eicker et al., 2024]. Although GIA uncertainty is often considered in glaciological studies [Velicogna et al., 2014, Groh and Horwath, 2021, Blazquez et al., 2018], it is still frequently neglected in hydrological applications, despite its influence in high-latitude regions (e.g., North America) [Eicker et al., 2024].

Ensemble-based and regional analyses further demonstrate that methodological choices made by different processing centres govern substantial parts of the GRACE(-FO) error budget. Blazquez et al. [2018] created an ensemble of 1500 post-processed gravity fields and showed that choices in geocentre treatment, GIA modelling, filtering, leakage correction, and data centre-specific conventions dominate uncertainties in global water- and sea-level trends. Regional analyses reinforce these findings: Velicogna et al. [2014] demonstrated that leakage, filtering, and background models substantially affect mass-balance estimates in Greenland and Antarctica, while Groh and Horwath [2021] showed similar impacts in Antarctica across multiple solutions. Complementary basin-scale and sea-level comparisons [Boergens et al., 2022, Ablain et al., 2019] further illustrate the consequences of differing processing conventions.

Another major source of uncertainty arises from the Atmosphere–Ocean De-Aliasing (AOD1B) background model. The AOD1B RL06 product is routinely removed prior to gravity field estimation [Dobslaw et al., 2017]. Recent work by Shihora et al. [2024] provides a quantification of residual AOD1B RL07 errors via the AOe07 time series, constructed

from ensemble simulations using different models of atmospheric and oceanic mass variability. They further provide a full spatio-temporal covariance matrix for these errors up to degree/order 40. Including AOD model uncertainties in gravity inversion has been shown to significantly reduce aliasing artefacts: Kvas and Mayer-Gürr [2019] demonstrated RMS noise reductions of $\sim 25\%$ over the oceans using co-estimation of AOD errors, while Zhou et al. [2023] reported 26–65% reductions in simulations. These results underscore the importance of including AOD1B uncertainty in data assimilation and other geophysical applications.

In this study, we present TUD-L2B-EWH_UNC, a transparent Level-2B mass anomaly product derived from monthly GRACE and GRACE-FO SHC solutions. The product preserves the geophysical content of the Level-2 data while applying only the minimal required processing steps, namely spherical harmonic truncation, noise filtering, and mean field removal. Here, "processing" refers to the sequence of modelling and correction steps applied before and after the Level-2 stage. Pre-processing includes the modelling choices made during gravity field recovery from Level-1B observations, such as the use of the AOD1B model and the parametrisation of gravitational and non-gravitational forces. Post-processing refers to the transformations commonly applied to Level-2 SHC solutions in order to derive gridded mass anomalies, including filtering, replacement of low-degree coefficients using satellite laser ranging (SLR), inclusion of degree-1 (geocenter) variations, and corrections for GIA or tidal aliasing. Unlike standard Level-2B or Level-3 products, TUD-L2B-EWH_UNC provides both GIA-corrected and uncorrected fields, with GIA, geocentre motion, and tidal aliasing corrections distributed as separate components, allowing users to apply them selectively. A central innovation is a structured, layered uncertainty product in which contributions from individual pre- and post-processing stages are provided alongside the combined Level-2B grids. This directly addresses several limitations identified in the literature: gridded, spatio-temporally resolved uncertainty fields are provided rather than collapsed spatial or temporal estimates; AOD1B uncertainty is included as a traceable, separable layer based on the AOe07 characterisation [Shihora et al., 2024]; GIA uncertainty is explicitly quantified and provided separately, supporting applications beyond glaciology; and the layered structure exposes individual processing choices transparently, rather than absorbing them into a single product.

2 Data Sources

2.1 GRACE(-FO) Level-2 Solutions

To construct the combined GRACE(-FO) solution and its associated uncertainty from Level-2 spherical harmonic (SH) products [Bettadpur, 2018a], we use monthly gravity field solutions from several processing centres. These solutions are summarised in Table 1. All datasets were obtained from the ICGEM repository [Ince et al., 2019]. The GRACE solutions cover the mission period from April 2002 to June 2017, while the GRACE-FO solutions span from 2018 to the present.

To quantify the variability among monthly solutions, each field is reduced by subtracting the monthly COST-G RL02.1 solution [Jäggi et al., 2022], which serves as the ensemble reference. The resulting spread across solutions is used as a measure of the inter-centre uncertainty, as described in Section 3.3.1.

Table 1: Monthly GRACE and GRACE-FO Level-2 spherical harmonic solutions used in this study. All solutions were downloaded from the ICGEM repository (`https://icgem.gfz-potsdam.de`). The COST-G RL02.1 solution is used as the ensemble reference.

Institute	Model name	Version	Max degree	Reference
ITSG	ITSG-Grace2018(_op)	–	60	Mayer-Gürr et al. [2018]
CSR	CSR	RL06 (06.3)	60	Bettadpur [2018b]
JPL	JPL	RL06	60	Yuan [2018]
GFZ	GFZ	RL06 (06.3)	60	Dahle et al. [2019]
HUST	HUST-Grace2024	–	60	Zhou et al. [2024]
LUH	LUH-Grace(-FO)-2020	–	96	Koch et al. [2021]
CNES	CNES CHOL	RL05	90	Lemoine and Bourgogne [2020]
AIUB	AIUB G3P	–	90	Darbeheshti et al. [2023]
AIUB	AIUB-GRACE-FO	RL02_op	90	Lasser et al. [2023]
APM-SYSU	APM-SYSU	–	90	Jäggi et al. [2022], Ince et al. [2019]
Tongji	Tongji-Grace2022	–	60	Chen et al. [2023]

2.2 Additional input data

Additional datasets include the Atmosphere and Ocean De-aliasing (AOD1B) error residuals product (AOe07), available for the period 2002–2020 [Shihora et al., 2024], and a set of 56 global Glacial Isostatic Adjustment (GIA) models compiled by Bagge et al. [2023]. These datasets are incorporated to quantify contributions from background model uncertainties and post-processing effects.

Low-degree spherical harmonic coefficients are treated using external Satellite Laser Ranging (SLR) solutions. The "oblateness" and d/o (3,0) coefficients, $C_{2,0}$ and $C_{3,0}$, respectively, are replaced using the official GRACE(-FO) Technical Note time series derived from SLR observations [Loomis and Rachlin, 2023]. Degree-1 (geocentre) coefficients are introduced using the standard geocentre solutions consistent with GRACE(-FO) Level-2 processing conventions [Swenson et al., 2008].

3 Methodology

3.1 From Level-2 to gridded Level-2B products

All Level-2 spherical harmonic (SH) solutions used in this study (see Section 2.1) are used up to degree and order (d/o) 60. For solutions provided at higher resolution (e.g., d/o 90 or 96), the Gentle Truncator (Barthelmes, accessed 17 December 2025) is applied to smoothly taper the SH coefficients from d/o 60 to zero at the maximum available degree, avoiding a sharp spectral cut.

To remove the long-term static component and isolate the time-variable signal, we subtract a static gravity field from each monthly solution. We adopt CSR's GGM05C [Ries et al., 2016], gently truncated from d/o 60 to 180, with a reference epoch of January 2008. A different choice would only shift the reference epoch, leaving the relative time-variable anomalies unchanged. Furthermore, the choice of static field does not affect the uncertainty characterisation: since all contemporary static gravity models are of equivalent quality up to d/o 60 [Ghobadi-Far et al., 2022]. Subsequently, DDK filtering [Kusche et al., 2009] of varying strengths (DDK2–DDK7) is applied to mitigate noise and leakage effects.

Certain low-degree coefficients require special treatment due to their importance for geophysical interpretation:

- The $C_{2,0}$ (for GRACE and GRACE-FO) and $C_{3,0}$ (for GRACE-FO) coefficients are replaced by satellite laser ranging-based values from TN-14v3 [Loomis and Rachlin, 2023, Loomis et al., 2020], because these low-degree terms are poorly constrained by GRACE/GRACE-FO data alone and strongly influence large-scale mass changes such as polar ice sheets, ocean mass redistribution, and land hydrology at high latitudes.
- The geocenter motion (degree-1) components is provided using TN-13 [Swenson et al., 2008], and is provided as a separate variable which can be optionally added by the user to the Level-2B grids. This term is essential for capturing mass variations relative to the Earth's centre of mass, which are most critical for oceanography and hydrological, glaciological, and solid Earth studies, focused on total error budgets.

Finally, the truncated and filtered SH coefficients are then synthesised to the spatial domain to obtain equivalent water height (EWH), δh, on a regular grid. For a degree-truncated solution at $n_{\max}$, the EWH at latitude θ and longitude λ is computed as [Ditmar, 2018]:

$$\delta h(r,\lambda,\theta) = \frac{M_E}{4\pi R^2 \rho_w} \sum_{n=1}^{n_{\max}} \sum_{m=0}^{n} \left(\frac{R}{r}\right)^{n+2} \frac{(2n+1)}{(1+k_n)} \left(\Delta\bar{C}_{nm}\cos m\lambda + \Delta\bar{S}_{nm}\sin m\lambda\right) \bar{P}_{nm}(\sin\theta), \tag{1}$$

where M_E is the Earth's mass, R is the mean Earth radius, r is the radial distance to the evaluation point on the reference ellipsoid, ρ_w is the density of water, k_n are the load Love numbers, $\Delta\bar{C}_{nm}$ and $\Delta\bar{S}_{nm}$ are the fully-normalised SH coefficient anomalies (w.r.t a static or long-term mean), and $\bar{P}_{nm}$ are fully-normalised associated Legendre functions. This formulation accounts explicitly for the ellipsoidal shape of the Earth and is consistent with modern EWH computations from SH coefficients.

3.2 Treatment of Persistent Tides for Level-2B

In addition to the standard 161-day S_2 tidal aliasing correction typically applied in Level-2B products [Dahle et al., 2025], we recommend removing three additional persistent tides: S_1, P_1, and K_1, as well as the non-modelled radiational tide R_3 [Koch et al., 2024] (see Table 2). These tides introduce spurious signals into monthly GRACE(-FO) solutions. In particular, the K_1 tide has a relatively large amplitude ($\sim$3–5 cm) and an aliasing period of approximately

$\sim$7 years, which may alias into the true geophysical signal. R_3 removal has not been commonly performed in previous studies, but it was identified as a non-modelled tide with significant period and amplitude [Koch et al., 2024]. All other tides not included here have been shown to either have insignificant amplitudes or aliasing periods equal to or well below the monthly Nyquist limit (2 months), and therefore are neglected.

The tidal signals are removed from the EWH grids by co-estimating each tide simultaneously with a climatological model that includes a bias (A), linear trend (B), quadratic trend (C), annual (D and E), and semi-annual components (F and G): $\delta h^{\mathrm{clim}}(t) = A + Bt' + \frac{1}{2}Ct'^2 + D\sin(\omega_{\mathrm{clim}}t') + E\cos(\omega_{\mathrm{clim}}t')$
$+ F\sin(2\omega_{\mathrm{clim}}t') + G\cos(2\omega_{\mathrm{clim}}t') + \sum_{k=1}^{N_k} S_k\sin(\omega_k t') + C_k\cos(\omega_k t')$. where t is in years, $t' = t - t_{\mathrm{ref}}$ with $t_{\mathrm{ref}} = 2008.0$, $\omega_{\mathrm{clim}} = 2\pi$ rad yr^{-1}, and S_k and C_k are the coefficients of the k^{th} tide with aliasing frequency ω_k (see Table 2). The resulting sine and cosine coefficients, S_k and C_k respectively, for each tide are stored separately (with the climatological coefficients), allowing users to inspect or reintegrate the tidal contribution if needed. For completeness, the amplitudes of these persistent tidal constituents are briefly analysed in Section B.4.

Table 2: Persistent tides (tidal periods and aliasing periods) to be removed from Level-2B EWH. Values of the tidal periods are directly retrieved from Koch et al. [2024], with GRACE and GRACE-FO nodal rate $\dot{\Omega} = -0.134\ ^\circ\mathrm{day}^{-1}$ (see Appendix B), and Earth's sidereal rotation $\omega = 360.9856\ ^\circ\mathrm{day}^{-1}$.

Tide	Period [day]	Aliasing Period [day]
S_2	$0.500000 \pm 7.968 \times 10^{-6}$	160.6
P_1	$1.002751 \pm 2.320 \times 10^{-5}$	170.8
S_1	$1.000021 \pm 3.625 \times 10^{-8}$	319.1
K_1	$0.997275 \pm 2.548 \times 10^{-5}$	2630.0
R_3	$1.003542 \pm 3.838 \times 10^{-5}$	150.6

3.3 Ensemble-Based and Processing-Related Uncertainties

3.3.1 Ensemble-Based Uncertainty from Multiple GRACE(-FO) Centers

Ensemble statistics across multiple Level-2B solutions are used to estimate pre-processing uncertainties, where the differences mostly lie in the use of parametrisation strategies and ocean tide background models (see Table 3).

Here, we use the monthly COST-G RL02.1 product [Jäggi et al., 2022] as the reference benchmark, as it represents a combined solution derived from multiple processing centres and is therefore less susceptible to centre-specific noise than any individual solution. We estimate the Level-2B uncertainty as the unbiased weighted ensemble standard deviation of the solutions for each month (l-level DDK filtered),

$$\sigma^2_{\delta h_l,\mathrm{sols}} = \frac{1}{1 - \sum_{i=1}^{N} \bar{w}^2_{l,i}} \sum_{i=1}^{N} \bar{w}_{l,i} \left(\delta h_{l,i} - \overline{\delta h_l}\right)^2, \tag{2}$$

where $\delta h_{l,i}$ denotes the monthly equivalent water height filtered value (with DDKl) for the i^{th} solution, $\overline{\delta h_l}$ is the weighted ensemble mean of the monthly solutions, N is the number of data centers ($N = 7$, see Section 2.1), and lastly $\bar{w}_{l,i}$ are the normalised weights computed using the square inverse of the monthly RMS over the oceans ($RMS_{\mathrm{oc},i}$) of the residuals w.r.t COST-G:

$$\bar{w}_{l,i} = \frac{1/RMS^2_{\mathrm{oc},i}}{\sum_i^N 1/RMS^2_{\mathrm{oc},i}}. \tag{3}$$

The use of the (weighted) ensemble standard deviation as an uncertainty estimator is supported by the statistical properties of the Level-2B residual distributions. As shown in Appendix A, residuals of all solutions with respect to the ensemble mean exhibit near-zero medians (of order 10^{-2} cm) and comparable distribution widths, indicating the absence of systematic offsets between data centers.

Not all solutions presented in Section 2.1 exhibit comparable noise characteristics, and a selection is therefore required to avoid contaminating both the combined ensemble mean and its associated uncertainty with solutions that display persistently elevated noise levels or outlier behaviour. To this end, we adopt as a selection metric the temporal and spatial (i.e. total) RMS of $\sigma_{\delta h_4,\mathrm{sols}}$ (Eq. 2), denoted as $\Delta RMS^{\mathrm{tot}}$, computed using a DDK4 filter. This filter level represents a compromise between limiting signal attenuation and retaining sufficient sensitivity to noise [Qian et al., 2022], thereby allowing the metric to predominantly reflect solution noise rather than filtering artefacts. Figure 1 shows the relative change in the average RMS for scenarios in which a single or multiple solutions are excluded, compared

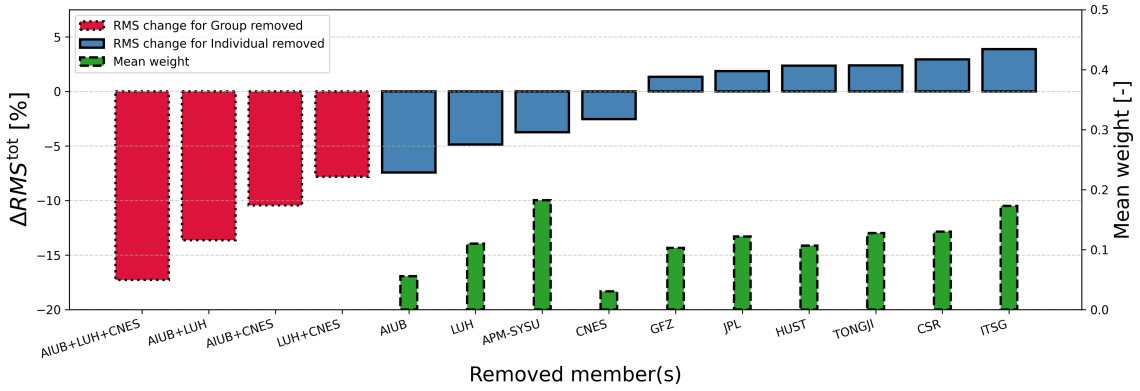

Figure 1: Relative difference in the total (spatio-temporal) root-mean-square, $\Delta RMS^{\mathrm{tot}}$, of the standard deviation for all Level-2B GRACE/GRACE-FO solutions (filtered using DDK4), computed when solutions are excluded relative to the case including all solutions. The COST-G RL02.1 solution is used as the benchmark to remove the monthly geophysical signal. The corresponding mean weights, calculated as the normalised inverse of the open ocean RMS, are also shown.

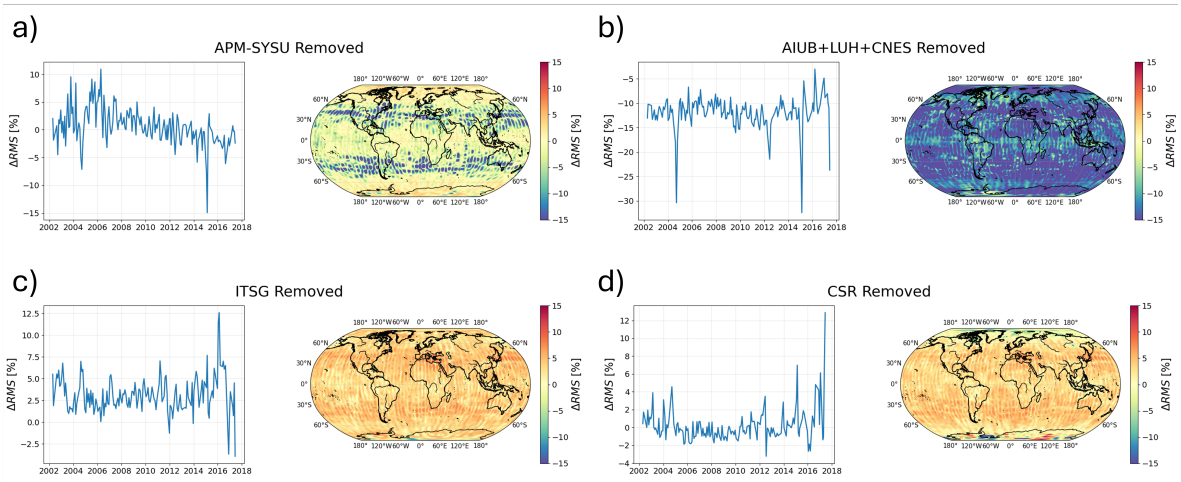

Figure 2: Relative difference in the time-dependent (left) and spatially distributed (right) RMS of the standard deviation for specific Level-2B GRACE/GRACE-FO solutions (filtered using DDK4), computed when one or more solutions are excluded relative to the case including all solutions. These removed solutions are: (a) APM-SYSU, (b) AIUB+LUH+CNES, (c) ITSG, and (d) CSR. The COST-G RL02.1 solution is used as the benchmark to remove the monthly geophysical signal.

to the nominal case where all solutions are retained. A negative relative $\Delta RMS^{\mathrm{tot}}$ indicates an improvement upon removal of the corresponding solution(s), whereas a positive value signifies a deterioration. The time average weights for each solution are also shown. Furthermore, Figure 2 shows the time and spatial ΔRMS for specific solutions, being APM-SYSU (Figure 2a), the AIUB, LUH and CNES combination (Figure 2b), ITSG (Figure 2c) and CSR (Figure 2d).

The most pronounced degradation is observed when removing the ITSG solution, which results in the largest positive change in total RMS, with $\Delta RMS^{\mathrm{tot}}$ raising to $+3.9\%$. This increase indicates a clear deterioration of the ensemble mean noise and highlights the contribution of ITSG within the combined product. This behaviour is corroborated by the spatial patterns shown in Figure 2c, where the relative RMS difference is predominantly positive, ranging from approximately $+2.5\%$ to $+5\%$ over most regions. Only during the final phase of the mission (from 11/2016 onwards) do isolated negative values of about -3% to -4% emerge. The overall dominance of positive spatial anomalies confirms that the removal of ITSG leads to a widespread increase in noise rather than isolated regional effects.

A qualitatively similar, though more nuanced, behaviour is observed for CSR, as shown in Figure 2d. In this case, the temporal evolution exhibits predominantly positive $\Delta RMS^{\mathrm{tot}}$ during non-nominal periods, in particular during

orbit repeat cycles, whereas during nominal mission phases the signal oscillates around 0%, with occasional negative excursions. This indicates that CSR performs very well in terms of noise handling during repeat patterns, data-limited, and other non-nominal intervals (with improvements ranging from 2% to 12%), while contributing more moderately during nominal conditions. The spatial distribution in Figure 2d further supports this interpretation, revealing distinct regional structures, most prominently in the Weddell Sea (approx. -12%) and in the vicinity of Greenland and Iceland. These coherent spatial patterns are characteristic of ocean tide model deficiencies and point to the ocean tide background model employed by CSR as the dominant source of its residual inconsistency. Consequently, the limitations associated with CSR are primarily linked to ocean tide modelling, while its overall performance during non-nominal mission phases remains excellent.

A particularly interesting case is the APM-SYSU solution. Despite having the largest ensemble weight of approximately 0.20, followed closely by ITSG with a weight of 0.17, its removal results in a negative $\Delta RMS^{\mathrm{tot}}$ of about -3.7%. This apparent contradiction is attributed to the temporal behaviour of APM-SYSU (see Figure 2a), which exhibits very low noise levels during nominal mission phases but significantly elevated noise during orbit repeat periods (see -8.7% and -15% on the 09/2004, and 02/2015) and months with reduced observational coverage (in 2003). A similar, albeit more pronounced, behaviour is observed for the LUH solution (not shown). Based on these considerations, we retain the APM-SYSU solution in the final ensemble, as its overall contribution remains beneficial ($+5\%$ to even $+10\%$ in $\Delta RMS^{\mathrm{tot}}$) during nominal conditions despite episodic degradation. In contrast, the AIUB, CNES, and LUH solutions are excluded from the combined product, as their removal leads to a substantial and robust reduction in ensemble noise.

In contrast, the removal of the AIUB solution yields the largest negative $\Delta RMS^{\mathrm{tot}}$ (approximately -7.5%), since it leads to the largest increase in ensemble noise over the oceans. Similarly, the LUH and CNES solutions also exhibit negative $\Delta RMS^{\mathrm{tot}}$ values when removed individually, indicating a net improvement in ensemble consistency. Motivated by these results, all possible combinations of two and all of these solutions were evaluated. The simultaneous removal of AIUB, CNES, and LUH leads to a pronounced reduction in $\Delta RMS^{\mathrm{tot}}$ of approximately -17.3%, representing the largest overall improvement among all tested combinations. This behaviour is clearly reflected in the temporal evolution shown in Figure 2b, where the relative RMS difference remains consistently negative throughout the mission. In particular, pronounced minima of approximately -30%, -22%, and -32% are observed during the orbit repeat and resonance periods around 09/2004, 06/2012, and 02/2015, respectively, with a similarly strong reduction of about -21% during the final month of the GRACE mission (06/2017). The spatial component exhibits a comparable behaviour, with predominantly negative values across the globe. On average, the spatial reduction amounts to approximately -15%, while locally enhanced reductions of up to -20% are observed during the same orbit repeat periods. Further combinations involving AIUB paired individually with CNES or LUH yield larger open ocean noise magnitude compared to the "LUH+CNES" case. These findings are consistent with the derived ensemble weights. Both AIUB and CNES exhibit relatively small weights below 0.06, reflecting their comparatively high noise levels, whereas LUH attains a larger weight of approximately 0.11, comparable in magnitude to GFZ and HUST. Notably, the latter two solutions display positive $\Delta RMS^{\mathrm{tot}}$ values when removed, further supporting their retention in the ensemble.

3.3.2 Background model pre-processing uncertainties

For the atmosphere–ocean background model contribution, we restrict our analysis to uncertainties arising from the AOD1B product. We do not explicitly model uncertainties from the ocean tide background model; instead, we assume that these are implicitly represented in the ensemble uncertainty (see Section 3.3.1) of the monthly GRACE/GRACE-FO solutions, as different processing centres rely on different ocean tide models (Table 3). Please note that at the moment of writing, we are unaware of any public documentation about the APM-SYSU GRACE solutions.

Table 3: Ocean tide models used in GRACE/GRACE-FO Level-2 processing across the selected analysis centres (see Section2.1). d/o refers to degree/order. (*) Additional co-estimation of residual ocean tide components (up to d/o 50) performed by TU Graz.

Analysis Centre	Ocean Tide Model	Max d/o	Reference
GFZ	FES2014	100	Carrère et al. [2016]
CSR	GOT4.8	180	Ray [2013]
JPL	FES2014b	180	Lyard et al. [2021]
TU Graz	FES2014b (*)	180	Lyard et al. [2021]
Tongji	EOT11a & FES2004	100	Savcenko and Bosch [2012], Lyard et al. [2006]
HUST	EOT11a	120	Savcenko and Bosch [2012]
APM-SYSU	N.A.	N.A.	N.A.

For the AOD1B component, we derive uncertainty fields from the AOe07 residual spherical harmonic coefficients of Shihora et al. [2024]. These 6-hourly fields are converted into equivalent water height (EWH), and the error estimate is

the monthly temporal root-mean-square as a spatially resolved (i.e. gridded) uncertainty estimate. The resulting EWH uncertainty fields are then propagated from Level-2 to Level-2B by applying the same filtering operators (DDK2–DDK7) used for the gravity solutions.

Although full L1B to L2 error propagation would, in principle, require applying the AOD1B residuals through the normal equations of each processing centre, this is not feasible within our framework. While normal matrices are available for some solutions (e.g. GFZ and ITSG), they are not available for all centres included in our ensemble (e.g. LUH, COST-G, HUST, Tongji, and APM-SYSU). Since our analysis is performed at the Level-2B stage (in EWH), a consistent propagation across all centres is not possible. We therefore follow the pragmatic approach to assume that additional amplification of AOD1B uncertainties during L1B to L2 processing is small compared with the dominant uncertainty sources represented in AOe07.

3.4 Post-processing uncertainties

Post-processing uncertainty in the GRACE(-FO) mass change estimates is dominated by three contributions: (i) propagated formal errors including the inserted degree-1 geocenter and the replacement of low-degree coefficients C20 and C30, (ii) uncertainty in the correction for glacial isostatic adjustment (GIA), and (iii) uncertainty associated with the spatial leakage correction. These components are treated as independent, as they originate from distinct physical processes and separate data sources.

3.4.1 Propagated formal errors of low-degree replacements

The formal errors from the SLR-based low-degree coefficient solutions [Swenson et al., 2008, Loomis and Rachlin, 2023] are propagated into equivalent water height (cm) as explained by Boergens et al. [2022]. This includes the inserted degree-1 geocenter and the replaced low-degree coefficients $C_{2,0}$ and $C_{3,0}$, as reported in the technical notes TN-13, and TN-14v3.

3.4.2 GIA trend uncertainty propagation

Uncertainty related to GIA corrections is treated separately. GIA trend uncertainty is quantified using ensemble statistics from 56 global GIA models compiled by Bagge et al. [2023], following the approach of Eicker et al. [2024]. The ensemble mean and standard deviation represent the current spread arising from uncertainties in Earth rheology and ice-history reconstructions. Since EWH fields are defined as temporal anomalies with respect to a reference epoch (t_{ref}), removal of a linear GIA trend introduces a time-dependent uncertainty into the anomaly time series. To ensure applicability across different geophysical use cases, the GIA trend uncertainty is provided in units of cm yr^{-1}, allowing users to propagate this uncertainty consistently for their specific choice of reference epoch.

3.4.3 Leakage correction uncertainty

Spatial filtering, while necessary to suppress noise in GRACE(-FO) solutions, inevitably attenuates true geophysical signals and introduces spectral leakage: energy from signals outside a region of interest bleeds into the estimate, and vice versa. To recover the attenuated signal, a leakage correction is applied, most commonly over regions with strong spatial contrasts such as coastlines or ice-sheet margins. However, the correction itself introduces uncertainty, since it depends on the assumed spatial distribution of the signal being recovered. We asses filtering-related uncertainty using the leakage-pair methodology introduced by Dobslaw et al. [2020] and applied to decorrelation filters of the DDK family [Kusche et al., 2009]. For a given filter level l, the partial leakage signal is defined as the difference between neighbouring filter strengths,

$$\lambda_l = \delta h_{l+1} - \delta h_{l-1}, \tag{4}$$

where δh_l denotes the equivalent water height field filtered with DDKl. The total leakage estimate is then obtained by scaling the partial leakage with a filter-specific coefficient,

$$\Lambda_l = c_l \, \lambda_l, \tag{5}$$

where the scale factor c_l accounts for the attenuation characteristics of the DDK filter and is determined empirically [Dobslaw et al., 2020]. The values for c_l used in this study are taken directly from [Dobslaw et al., 2020] and are listed in Table 4.

Table 4: Scaling coefficients c_l used for leakage estimation following Dobslaw et al. [2020].

Filter	DDK2	DDK3	DDK4	DDK5	DDK6	DDK7
c_l	2.9	3.9	4.5	4.0	4.5	4.4

Uncertainty in the leakage estimate arises from three sources: the ensemble solution spread across processing centers, the covariance between neighbouring filter strengths, and uncertainty in the scaling coefficient c_l. Using ensemble statistics across the multiple Level-2B solutions (Section 3.3.1), the variance of the partial leakage is given by

$$\sigma^2_{\lambda_l} = \sigma^2_{l+1} + \sigma^2_{l-1} - 2\,\mathrm{Cov}(\delta h_{l+1}, \delta h_{l-1})\,, \tag{6}$$

where σ^2_l denotes the ensemble variance of the DDKl-filtered solution. The covariance term is essential, as neighbouring DDK filters share a large fraction of their retained noise.

The variance of the total leakage estimate Λ_n is then obtained by standard error propagation of Eq. 5,

$$\sigma^2_{\Lambda_l} = c_l^2\,\sigma^2_{\lambda_l} + \lambda_n^2\,\sigma^2_{c_l}, \tag{7}$$

where $\sigma^2_{c_l}$ represents the uncertainty of the scaling coefficient itself. The first term reflects uncertainty due to ensemble solution variability and correlated filter responses. In contrast, the second term captures the sensitivity of the leakage estimate to imperfect knowledge of the filter attenuation characteristics. In the present study, c_l is taken as a fixed constant across ensemble members, times, and grid cells. Ideally, the uncertainty in c_l would also be included. While c_l is expected to have a relatively high uncertainty [Dobslaw et al., 2020], e.g. only for DDK3 different values are provided for the four processing centers (GFZ, CSR, JPL, ITSG: 3.9, 4.2, 4.4, 3.9) with a standard deviation of ~ 0.27, no information is available for other DDK filter levels or the additional solutions included in this study. Consequently, the total leakage variance is effectively given by the first term alone in Eq. 7, as

$$\sigma^2_{\Lambda_l} \approx c_l^2\,\sigma^2_{\lambda_l} \tag{8}$$

3.4.4 Total uncertainty

The total Level-2B 1σ-uncertainty of the GRACE and GRACE-FO EWH products (subscript δh omitted for brevity) combines the individual components as

$$\sigma^2_{\mathrm{GFO}}(t) = \sigma^2_{\mathrm{sols}}(t) + \sigma^2_{\mathrm{AOD1B}}(t) + \sigma^2_{\mathrm{geoc}}(t) + \sigma^2_{C_{2,0}}(t) + \sigma^2_{C_{3,0}}(t), \tag{9}$$

where, we assume that all components are statistically independent.

Here, $\sigma^2_{\mathrm{sols}}(t)$ represents the ensemble solution variability of the Level-2 gravity field solutions and captures uncertainties related to processing choices and background modelling across analysis centres. The term $\sigma^2_{\mathrm{AOD1B}}(t)$ accounts for residual errors in the atmosphere–ocean de-aliasing corrections applied during Level-1B to Level-2 processing. The contributions σ^2_{geoc}, $\sigma^2_{C_{2,0}}$, and $\sigma^2_{C_{3,0}}$ correspond to the propagated formal errors associated with the inserted degree-1 geocenter and the replaced low-degree coefficients, respectively. The SLR contributions are removed when using the "noSLR" ancillary product.

If the user applies leakage correction, the associated uncertainty $\sigma^2_{\Lambda_l}(t)$ should be added to account for filtering-induced effects. Lastly, when correcting for GIA, the user should add the GIA trend uncertainty to the trend of the corrected signal. The propagation of this uncertainty after GIA correction follows $\sigma_{\mathrm{GIA,trend}}|t - t_{\mathrm{ref}}|$, where t_{ref} is the reference epoch for climatological studies (see Section 3.2).

3.5 Regions of interest

Within this study, uncertainties are illustrated using three major river basins that span a wide range of climatic and hydrological regimes: the Amazon, the Ganges–Brahmaputra, and the Mississippi–Missouri basins. In addition, cryospheric uncertainty characteristics are demonstrated for the two largest ice sheets, Greenland and Antarctica. Finally, for oceanic mass variability, the Zapiola Rise is included as a representative region dominated by barotropic ocean dynamics. These regions can be found shaded in Figure 3.

4 Data Product Description

4.1 File Formats and Access

The dataset is distributed in NetCDF format, following the Climate and Forecast (CF) metadata conventions, which standardise variable names, units, coordinate systems, and attributes to ensure that files are self-describing and interoperable across software tools and disciplines. Separate files are provided for different DDK decorrelation filter strengths (DDK2–DDK7), allowing users to select an appropriate balance between noise reduction and spatial resolution.

The main data product follows the naming convention:

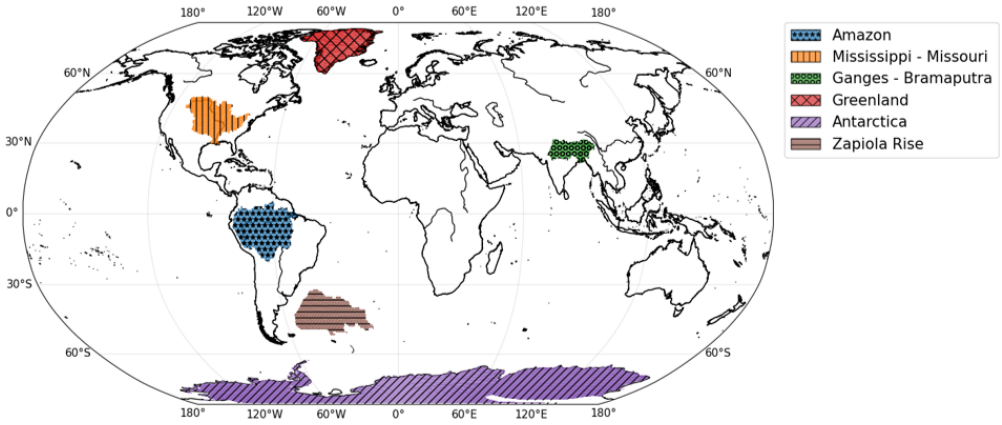

Figure 3: Geographic extent of the regions used to illustrate GRACE(-FO) uncertainty characteristics. Shown are the Amazon, Ganges–Brahmaputra, and Mississippi–Missouri river basins (hydrology), the Greenland and Antarctic ice sheets (cryosphere), and the Zapiola Rise (ocean). Regional geometries follow Dahle et al. [2025].

`TUD-L2B-EWH_UNC-GRACEv4-DDK{i}-2002_2020-0.5x0.5.nc`,

where i denotes the applied DDK filter level. Complementary to the main data product, an alternative set of files is provided in which low-degree spherical harmonic coefficients are not replaced by Satellite Laser Ranging (SLR) estimates. These files contain the ensemble solution uncertainty derived purely from the original GRACE(-FO) solutions and can be used by users to assess the impact of low-degree coefficient replacement. The corresponding files follow the naming convention:

`TUD-L2B-EWH_UNC_noSLR-GRACEv4-DDK{i}-2002_2020-0.5x0.5.nc`.

In addition, three ancillary climatological products (see Section 3.2) are provided:

`TUD-L2B-EWH_CLIM-GRACEv4-DDK{i}-2002_2020-0.5x0.5.nc`,

`TUD-L2B-EWH_CLIM_CORR-GRACEv4-DDK{i}-2002_2020-0.5x0.5.nc`,

and

`TUD-L2B-EWH_CLIM_LEAKAGE-GRACEv4-DDK{i}-2002_2020-0.5x0.5.nc`.

These files contain fitted climatological parameters, including bias, trend, acceleration, seasonal terms, and aliasing tidal coefficients, as described in Section 3.2. These parameters allow users to reconstruct climatological full or leaked signals and optionally remove dominant tidal aliasing contributions (e.g. S_2, P_1, and K_1), and other secondary contributors (i.e. S_1, and R_3), in post-processing.

Uncertainty components can be combined to form a total monthly GRACE(-FO) uncertainty using Eq. 9, while GIA corrections and their associated uncertainties can be applied separately, depending on the intended application. Comprehensive variable definitions, units, and usage examples are provided in the online README documentation accompanying the dataset.

4.2 Grid and Variables

The dataset is provided on a global 0.5 $\times$ 0.5 latitude–longitude grid, with dimensions $(\mathrm{time}, \mathrm{lat}, \mathrm{lon})$, and spans the period from April 2002 to December 2020. The current temporal coverage is limited by the availability of the AOe07 residual AOD1B uncertainty product [Shihora et al., 2024], which is provided up to December 2020. The dataset will be extended beyond this period once an updated AOe07 release becomes available. The primary geophysical variable is the equivalent water height, denoted as `ewh_mean`.

For each DDK filter strength, the product contains an ensemble weighted-mean EWH signal derived from multiple GRACE and GRACE-FO Level-2 solutions.

4.2.1 Main GRACE(-FO) Product

The main variables included in the `TUD-L2B-EWH_UNC-GRACE` product are:

- `ewh_mean`: ensemble weighted-mean EWH signal [cm],
- `ewh_mean_corr`: `ewh_mean` corrected for GIA (reference epoch: 2008.0), geocenter motion, and aliasing tides [cm],
- `ewh_mean_leakage`: ensemble weighted-mean leakage correction uncertainty (Λ_l, see Eq. 5) [cm],
- `ewh_degree1`: degree-1 (geocenter) EWH contribution [cm],
- `ewh_unc_sols`: ensemble solution uncertainty ($\sigma_{\delta h_l,\mathrm{sols}}$, see Eq. 2) [cm],
- `ewh_unc_aod1b`: atmosphere–ocean background model uncertainty [cm],
- `ewh_unc_leakage`: total leakage correction uncertainty (σ_{Λ_l}, see Eq. 8) [cm],
- `ewh_unc_degree1`: propagated degree-1 uncertainty [cm],
- `ewh_unc_degree20`: propagated $C_{2,0}$ uncertainty [cm],
- `ewh_unc_degree30`: propagated $C_{3,0}$ uncertainty [cm],
- `ewh_gia_mean`: ensemble mean GIA trend [cm yr^{-1}],
- `ewh_gia_unc`: GIA trend uncertainty [cm yr^{-1}],
- `weights`: normalised, time-dependent ensemble weights ($\bar{w}_{l,i}$, see Eq. 3) used to compute the weighted ensemble mean and associated uncertainties, provided for each contributing solution with dimensions $(\mathrm{time}, \mathrm{member})$.

All EWH grids contain time-variable gravity signals represented by spherical harmonic degrees 2 to 60. Degree-1 (geocenter) contributions are provided separately in the variable `ewh_degree1` and may be added by the user if required. For clarity, Appendix C (Table 8) summarises which geophysical components (degree-1, $C_{2,0}$, $C_{3,0}$, and higher degrees) are represented in each variable. We also provide the ensemble weights (see Eq. 3) are explicitly provided as part of the data product. The `member` dimension corresponds to the string identifier of each contributing Level-2B solution (i.e. the originating data center), allowing users to reconstruct (using Eq. 2) the ensemble mean and uncertainty estimates exactly.

4.2.2 NoSLR Ancillary Product

A minimal ancillary product is provided for analyses requiring SLR-free ensemble statistics. The `TUD-L2B-EWH_UNC_noSLR-GRACE` files contain:

- `ewh_mean`: ensemble weighted-mean EWH signal with no SLR replacement [cm],
- `ewh_unc_sols`: ensemble solution uncertainty with no SLR replacement [cm],
- `weights`: normalized, time-dependent ensemble weights with dimensions $(\mathrm{time}, \mathrm{member})$.

This product is intentionally small, containing only variables needed to perform SLR-free analyses while reproducing the weighted ensemble mean and uncertainty estimates (using Eq. 2). The geophysical content of this ancillary product is summarised in Appendix C (Table 9).

4.2.3 Climatology Products

In addition to the Level-2B gridded product, two `CLIM` ancillary products are provided to enable climatological reconstruction of the EWH signal. The two main climatological products, `TUD-L2B-EWH_CLIM-GRACE` and `TUD-L2B-EWH_CLIM_CORR-GRACE`, share an identical variable structure. Throughout this section, the prefix `var` appearing in variable names refers to `ewh_mean` in the uncorrected product (`TUD-L2B-EWH_CLIM-GRACE`) and to `ewh_mean_corr` in the fully post-processed product (`TUD-L2B-EWH_CLIM_CORR-GRACE`); for example, `var_beta` becomes `ewh_mean_beta` or `ewh_mean_corr_beta`, respectively. Both products contain the following variables:

- `var_beta`: gridded climatological regression coefficients with dimensions $(\mathrm{lat}, \mathrm{lon}, \mathrm{coeff})$,
- `var_beta_std`: unbiased standard deviation of the post-fit residuals between the ensemble-mean EWH time series and its fitted climatological model, i.e. the square root of the unbiased variance of $\left(\overline{\delta h_l}(t) - \delta h_l^{clim}(t)\right)$.

- `t_clim`: numeric time variable compatible with the regression model, expressed in fractional years and centered at 2008.0,
- `var_clim`: climatological fit ($\delta h_l^{\mathrm{clim}}$) of the ensemble weighted-mean EWH signal in [cm], with dimensions $(\mathrm{time}, \mathrm{lat}, \mathrm{lon})$.
- `var_tides`: climatological tidal aliasing fit of the ensemble weighted-mean EWH signal in [cm], with dimensions $(\mathrm{time}, \mathrm{lat}, \mathrm{lon})$.
- `residuals`: difference between climatology and ensemble mean $\left(\overline{\delta h_l}(t) - \delta h_l^{clim}(t)\right)$ in [cm], with dimensions $(\mathrm{time}, \mathrm{lat}, \mathrm{lon})$.

The `coeff`-dimension of the `var_beta` variable enumerates the regression parameters used to describe the long-term, seasonal, and tidal variability of the EWH signal (see Eq. 3.2). It includes the following components:

- `bias`: constant offset term [cm],
- `trend`: linear trend coefficient [cm yr^{-1}],
- `acc`: quadratic (acceleration) term [cm yr^{-2}],
- `annual_cos`, `annual_sin`: annual harmonic terms [cm],
- `semiannual_cos`, `semiannual_sin`: semiannual harmonic terms [cm],
- `{tide}_cos`, `{tide}_sin`: cosine and sine coefficients [cm] associated with selected tidal constituents (S_2, P_1, K_1, S_1, and R_3).

Together, `var_beta` and `t_clim` allow users to reconstruct the climatological EWH signal using Eq. 3.2, consistently with the time dimension of the main product. The time variable `t_clim` can also be used to remove GIA from the GRACE(-FO) signal (i.e. `var`). The same variable naming convention applies to the leakage climatological ancillary product
`TUD-L2B-EWH_CLIM_LEAKAGE-GRACE`, which allows users to evaluate the effect of leakage on the climatological fit by adding this contribution to the main climatological fit.

5 Results

5.1 Comparison of TUD-L2B Ensemble Mean with Existing Products

To validate our combined methodology, we compute the spatial RMS over the open oceans for each DDK filter level. Prior to this calculation, deterministic signals are removed by fitting and subtracting a climatological model comprising a bias, linear trend, quadratic term, annual and semi-annual components, and the dominant tidal aliases. The open ocean is then used as a noise proxy, on the assumption that once these systematic contributions are accounted for, any remaining signal reflects noise rather than true geophysical variability.

The RMS is evaluated over oceanic regions that are expected to contain minimal geophysical signal. To ensure this, a 500-km buffer is applied to exclude land and coastal influences, and the Argentine Basin is additionally masked to suppress residual variability associated with the oceanic gyre. The remaining oceanic signals are therefore assumed to empirically represent the intrinsic solution noise as a function of time, as seen in Figure 4. For reference, the individual solutions from CSR, JPL, GFZ, and ITSG, as well as the COST-G combination, are included in the figure alongside the TUD ensemble mean. Furthermore, a sensitivity analysis is performed on the influence of DDK filter level, where for each filter strength the open ocean RMS is averaged over the full temporal record of each data centre solution and visualised in Figure 5.

From Figure 4, we observe that for the widely used DDK3 filter [Kusche et al., 2009, Werth et al., 2009, Qian et al., 2022], the TUD ensemble mean exhibits the lowest average open-ocean RMS of 1.62 cm. Comparable performance is obtained by ITSG-Grace2018 and COST-G (~ 1.77 cm), followed by CSR (~ 2.00 cm), JPL (~ 2.21 cm), and finally GFZ ((~ 2.30 cm)). This ranking is further corroborated by Figure 5, which summarizes the temporal mean RMS as a function of DDK filter level.

A notable feature is that the combined COST-G (RL02.1) solution exhibits elevated noise levels above 4 cm during orbit repeat periods (notably around 09/2004 and 02/2015, with RMS values of 4 and 10 cm, respectively), exceeding those of all other solutions by a factor of two. We hypothesise that this behaviour is primarily related to the inclusion of the APM-SYSU solutions in the COST-G ensemble. While APM-SYSU demonstrates low noise levels during nominal periods (with a $\Delta RMS^{\mathrm{tot}}$ from 5 to 10%), it exhibits some of the highest RMS values during orbit repeat patterns (see Section 3.3). In contrast, the TUD-L2B ensemble mean maintains low RMS levels during these repeat periods. This

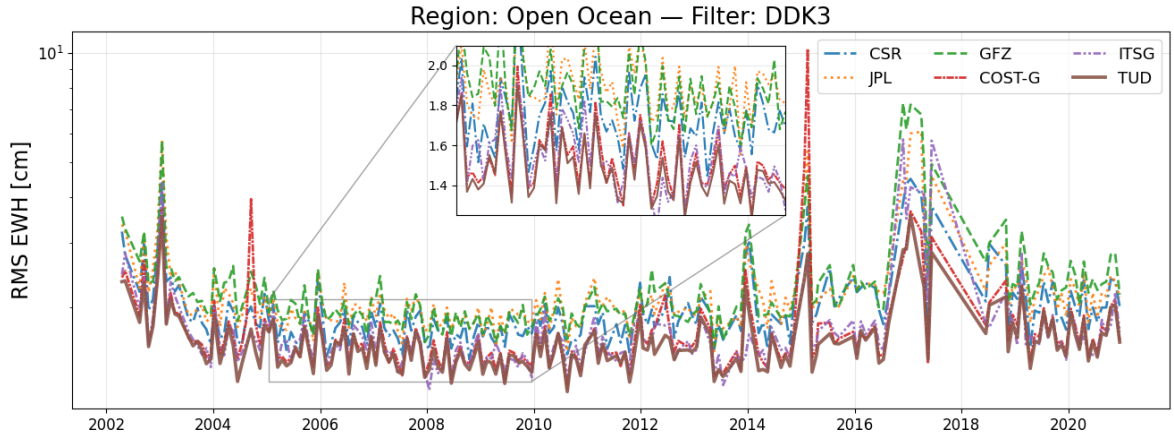

Figure 4: Spatial RMS over the open oceans for the five most recent Level-2B GRACE/GRACE-FO solutions (CSR, JPL, GFZ, ITSG, and the combined COST-G), compared against the TUD-L2B ensemble mean. A DDK3 filter is applied, together with a 500 km coastal buffer and an additional mask over the Argentine ocean basin.

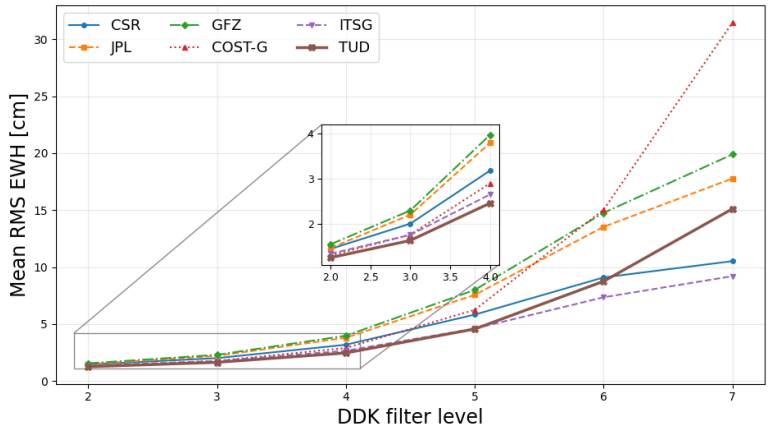

Figure 5: Temporal mean of the open-ocean spatial RMS as a function of DDK filter level for the five most recent Level-2B GRACE(-FO) solutions (CSR, JPL, GFZ, ITSG, and the combined COST-G), compared with the TUD-L2B product.

behaviour is largely consistent across DDK filter levels. For DDK levels 2 through 6, the TUD-L2B ensemble mean yields the lowest mean EWH RMS among all solutions (Figure 5), with the exception of DDK6, where its RMS ($\sim$8.7 cm) is marginally higher than that of ITSG ($\sim$7.4 cm). As expected, COST-G exhibits RMS values of 1.30 and 1.77 cm for DDK2–3, respectively, similar to ITSG. From DDK4 onward, however, COST-G shows a systematic 1 cm increase in RMS, most likely driven by enhanced noise during orbit repeat periods, and reaches values comparable to CSR ($\sim$ 5 cm) at DDK5. For the weakest filtering levels (DDK6–7), COST-G displays a pronounced RMS increase relative to DDK5, becoming the noisiest solution, with RMS values reaching up to 15–31 cm.

A similar, though less pronounced, behaviour is observed for the TUD ensemble mean at DDK7, where its RMS of 15 cm exceeds that of CSR ($\sim$10.5 cm) but is lower than JPL ($\sim$18 cm). This outcome is expected, as the ensemble weights are defined relative to COST-G. Consequently, as filter strength decreases (from DDK4 to DDK7), noise contributions associated with COST-G become increasingly influential. Furthermore, the same analysis has been performed over the Sahara and Gobi deserts, two geophysically quiet regions (not shown here), confirming the observed results. Overall, these results indicate that the combined product is stable across DDK filter strengths and support the validity of the ensemble-mean approach used in this study.

5.2 Uncertainty Results

5.2.1 AOD1B uncertainty

As previously mentioned, the uncertainty associated with the AOD1B de-aliasing product is defined as the temporal RMS within each month of the 6-hourly AOe07 model fields. This approach provides an estimate of the residual atmosphere–ocean variability that is not removed during the de-aliasing step. In the following, we analyse the temporal RMS of the monthly AOD1B uncertainties over the period 2002–2020.

Figure 6 shows the spatial distribution of these uncertainties for the case of DDK3-filtered solutions. Although the dataset provides equivalent estimates for the full range of DDK filters (DDK2–DDK7), the DDK3 case is shown here as a representative example commonly used in geophysical applications.

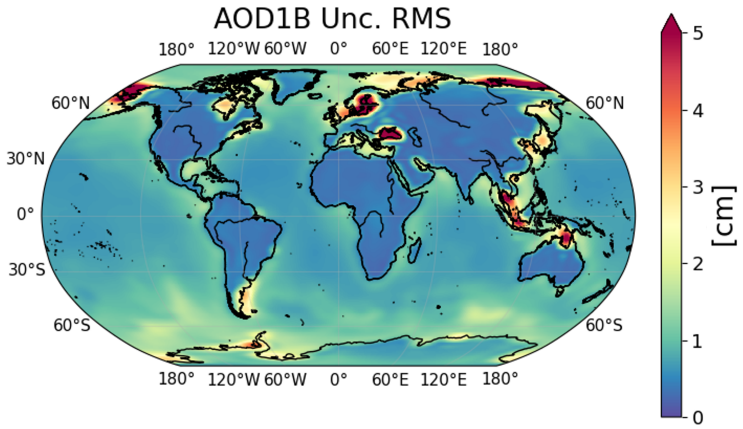

Figure 6: Spatial distribution of AOD1B uncertainty computed from the AOe07 spherical harmonic coefficients propagated to equivalent water height (EWH) and filtered with DDK3 (degree and order 2–60). The global mean RMS over 2002–2020 is 1.04 cm EWH.

The resulting AOD1B uncertainty field exhibits a global mean RMS of approximately 1.04 cm EWH, confirming that it represents a secondary but non-negligible contribution to the overall uncertainty budget. However, the spatial distribution is strongly inhomogeneous. Elevated values are predominantly observed along coastal zones and marginal seas, where residual atmosphere–ocean mass exchange and model sensitivity are largest. In these regions, RMS values locally reach 3–5 cm. In contrast, uncertainties over continental interiors are substantially smaller and typically remain below 0.5 cm, reflecting the reduced influence of oceanic mass variability and the greater stability of the atmospheric component over land.

5.2.2 GIA ensemble statistics

Glacial Isostatic Adjustment (GIA) uncertainty is quantified using an ensemble of 56 global GIA models compiled by Bagge et al. [2023], following the same methodology as in Eicker et al. [2024]. The ensemble spans a wide range of Earth rheology and ice-history assumptions and therefore provides a representative measure of current model uncertainty. For each grid point, we compute the ensemble mean GIA signal, the standard deviation (1σ), as well as the minimum and maximum deviations relative to the ensemble mean. The ensemble mean is used as the best-estimate GIA correction, while the ensemble standard deviation reflects uncertainty arising from structural and ice-history model differences. The minimum and maximum deviations are included to capture the full range of plausible model outcomes, highlighting regions where GIA predictions diverge most strongly across the ensemble.

The uncertainty estimation is performed consistently for multiple decorrelation filter settings (DDK2–DDK7), allowing users to apply the corresponding GIA uncertainty fields together with the associated DDK-filtered TUD-L2B ensemble means or with any other GRACE(-FO) solution processed using the same filter. Figure 7 shows an example of the resulting ensemble statistics for the DDK3-filtered GIA fields, illustrating the spatial distribution of the ensemble mean (Figure 7a), standard deviation (Figure 7b), and extreme deviations (Figure 7c,d). Regions of particularly large GIA uncertainty coincide with formerly glaciated areas, such as North America, Northern Europe (Scandinavia), and polar regions such as Southern Greenland, and Antarctica, whereas low-latitude regions exhibit comparatively small ensemble spread. Typical standard deviations (Figure 7b) are approximately 1.2–2 $\mathrm{cm\ yr^{-1}}$ in North America, 0.5–0.9 $\mathrm{cm\ yr^{-1}}$ in Northern Europe, 1.5–2 $\mathrm{cm\ yr^{-1}}$ in Southern Greenland, and around 0.5 $\mathrm{cm\ yr^{-1}}$ in Antarctica, with localized regions reaching 0.6 $\mathrm{cm\ yr^{-1}}$.

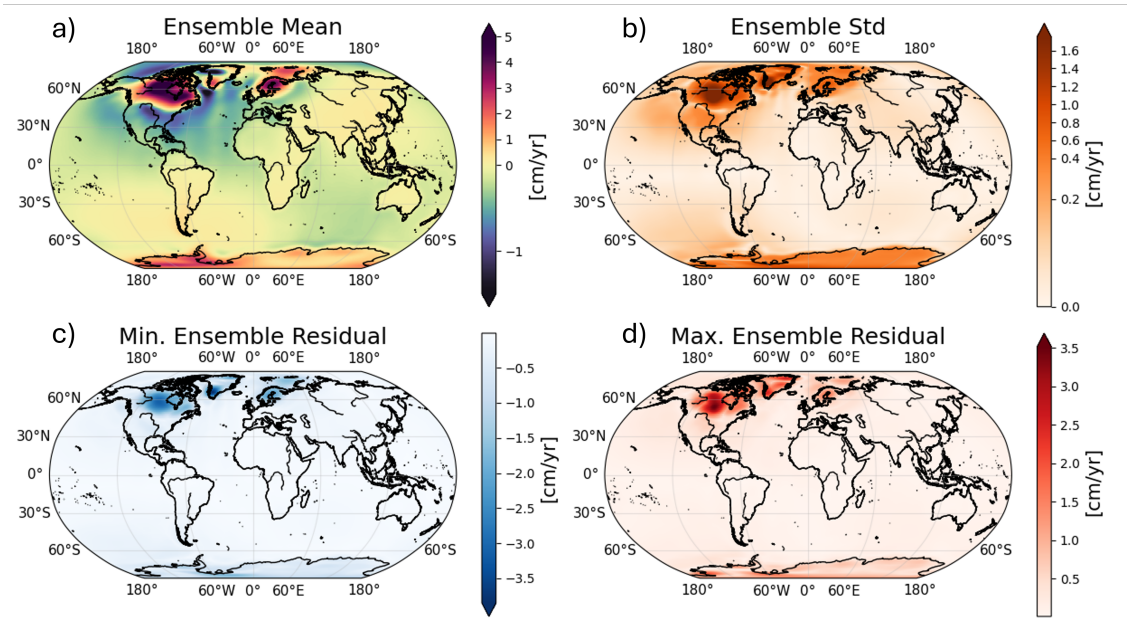

Figure 7: Ensemble statistics of Glacial Isostatic Adjustment (GIA) derived from 56 global GIA models [Bagge et al., 2023] (filtered using DDK3). Shown are the ensemble mean (a), standard deviation (b), and the minimum and maximum deviations relative to the ensemble mean (c,d).

5.2.3 Hydrology applications

Hydrological mass variations are characterised by large-amplitude seasonal signals combined with pronounced interannual variability. To assess the performance of the ensemble approach in this context, time series of EWH are analysed for three major river basins: the Amazon, the Ganges–Brahmaputra, and the Mississippi–Missouri (see Figure 3). All solutions have been corrected for the ensemble-mean GIA signal and for aliased tidal constituents, while the degree-1 geocentre signal has been added, and the low-degree SLR coefficients have been updated to replace the corresponding components in the original solutions.

For each basin, basin-averaged EWH time series are extracted from selected Level-2B solutions and compared with the TUD-L2B ensemble mean. Uncertainty envelopes shown in Figure 8 represent $\pm 2\sigma$ (approximately 95% confidence) contributions from three components: ensemble solution uncertainty, AOD1B uncertainty, and the combined low-degree replacement uncertainty (degree-1 and SLR-derived $C_{2,0}$ and $C_{3,0}$). The $\pm 2\sigma$ interval is adopted here as a representative visualisation; all uncertainty components are provided in the data product as standard deviations, allowing users to construct application-specific confidence levels. The ensemble mean is shown together with five solutions (CSR, JPL, GFZ, ITSG, and COST-G). Basin-mean EWH characteristics and GIA trend statistics are summarised in Table 5.

Table 5: Basin-averaged characteristics of equivalent water height (EWH) variability and GIA correction (DDK3 filtered, degree/order 2–60). Shown are the annual amplitude and linear trend estimated from the GRACE(-FO) EWH (GIA-uncorrected) time series, together with the ensemble-mean GIA trend and its associated uncertainty derived from 56 global GIA models [Bagge et al., 2023].

Basin	Annual Amplitude [cm]	Trend [cm yr^{-1}]	GIA [cm yr^{-1}]	GIA uncertainty [cm yr^{-1}]
Amazon	19.0	0.29	0.01	0.02
Mississippi–Missouri	4.56	0.085	−0.70	0.30
Ganges–Brahmaputra	13.0	-1.11	0.20	0.08

For the Amazon and Ganges–Brahmaputra basins, both the ensemble-mean GIA trend and its associated uncertainty are small, remaining below 0.1 cm yr^{-1}. Even when accumulated over a decade, the corresponding GIA uncertainty remains below $\sim$ 1 cm and is negligible compared to the seasonal amplitudes of approximately 19 cm and 13 cm, respectively. In addition, the ensemble-mean GIA trends (0.01 and 0.20 cm yr^{-1}) are small relative to the observed EWH trends, indicating that GIA corrections play a minor role in the interpretation of long-term hydrological variability in these basins. In contrast, the Mississippi–Missouri basin exhibits a substantially larger ensemble-mean GIA trend

(-0.70 cm yr^{-1}) and associated uncertainty (0.30 cm yr^{-1}). Over a decadal timescale, this uncertainty accumulates to approximately 3 cm, which is comparable to the basin's seasonal amplitude (4.6 cm) and exceeds the uncorrected EWH trend (0.085 cm yr^{-1}). As a result, GIA-related uncertainty becomes a non-negligible contributor to trend interpretation in this basin. A similar behaviour is observed for the Mackenzie River basin (not shown), which is located closer to the centre of the GIA signal in northern North America. There, the ensemble-mean GIA trend amounts to 2.81 ± 1.02 cm yr^{-1}, compared to an annual amplitude of 3.17 cm and an observed EWH trend of 1.20 cm yr^{-1}. In this case, both the magnitude and uncertainty of the GIA correction are comparable to, or exceed, the hydrological trend itself.

Considering the remaining uncertainty components, ensemble solution uncertainty constitutes the dominant contribution in all three basins. When expressed at the $\pm 2\sigma$ level, it reaches approximately 2.5–3.5 cm, reflecting differences among processing centres, background models, and noise characteristics. AOD1B uncertainty and the combined low-degree replacement uncertainty are smaller but comparable in magnitude, each contributing approximately 0.6–0.8 cm at the $\pm 2\sigma$ level.

Detailed basin-averaged statistics of ensemble solution uncertainty, AOD1B uncertainty, and combined low-degree replacement uncertainty are provided in Appendix D.1 (Table 10). These statistics confirm that ensemble uncertainty dominates the uncertainty budget for large river basins, while AOD1B and low-degree uncertainties form secondary but non-negligible contributions. Overall, the results demonstrate that, although GIA uncertainty is negligible for most low-latitude hydrological basins, robust interpretation of seasonal and interannual variability requires explicit consideration of ensemble uncertainty together with background-model-related uncertainties.

5.2.4 Glaciology applications

Glaciological mass-change signals are dominated by long-term trends, with comparatively small seasonal components. This places strong requirements on the treatment and propagation of low-frequency errors. We therefore focus on the two largest ice sheets, Antarctica and Greenland, to assess the performance of the ensemble approach for cryospheric mass-balance applications. Using the same methodology as in the previous sections, spatially averaged mass-change time series are derived from each Level-2B solution and compared with the TUD-L2B ensemble mean. Figure 9 shows the resulting time series together with their associated $\pm 2\sigma$ (95%) uncertainty envelopes, explicitly illustrating the relative contributions of ensemble solution uncertainty, AOD1B uncertainty, and the combined low-degree (degree-1 and SLR) uncertainty. Region-averaged GIA trend statistics are reported separately in Table 6.

Table 6: Region-averaged characteristics of equivalent water height (EWH) variability and GIA correction (DDK3 filtered, degree and order 2–60) for Greenland and Antarctica. Shown are the annual amplitude, absolute minimum–maximum range, and linear trend estimated from the GRACE(-FO) EWH (GIA-uncorrected) time series, together with the ensemble-mean GIA trend and its associated uncertainty derived from 56 global GIA models [Bagge et al., 2023].

Region	Ann. Amplitude [cm]	|Min–Max| [cm]	Trend [cm yr^{-1}]	GIA trend [cm yr^{-1}]	GIA uncertainty [cm yr^{-1}]
Greenland	2.7	114.83	-6.3	0.19	0.86
Antarctica	0.68	6.24	-0.11	1.10	0.45

For Antarctica (Figure 9a), the ensemble uncertainty represents the dominant uncertainty contribution, with 95% confidence levels reaching approximately 1.4–4.0 cm. AOD1B uncertainty forms the second largest component, contributing at the level of approximately 2–4 cm. The combined low-degree uncertainty associated with degree-1 and SLR coefficients is substantially smaller, with a typical 95% confidence magnitude of about 1.0–1.2 cm.

A similar hierarchy is observed for Greenland (Figure 9b). Here, ensemble uncertainty again dominates, with 95% confidence levels of approximately 2.0–5.0 cm, followed closely by AOD1B uncertainty at roughly 1.6–3.0 cm. The combined degree-1 and SLR uncertainty remains the smallest contribution, with magnitudes comparable to those found for Antarctica (approximately 1.0–1.2 cm).

Comparing these uncertainties to the magnitude of the observed mass-change signals highlights their relevance for glaciological applications. For Antarctica, where the basin-averaged signal range is relatively small ($|\text{min–max}| = 6.24$ cm), the ensemble uncertainty and AOD1B uncertainties already constitute a substantial fraction ($\sim 26.3\%$) of the total signal variability. In addition, the ensemble-derived GIA trend uncertainty of 0.45 cm yr^{-1} (Table 6) propagates into several centimetres over decadal time scales, becoming comparable to the dominant Level-2B uncertainty contributions. In Greenland, although the absolute mass-change signal is much larger ($|\text{min–max}| = 114.83$ cm), ensemble uncertainty and AOD1B uncertainties remain non-negligible ($\sim 1.5\%$) and must be accounted for in trend analyses. Here, the larger GIA trend uncertainty of 0.86 cm yr^{-1} similarly accumulates over time and directly impacts (by $\sim 7.5\%$) long-term mass-balance estimates. In contrast, the combined low-degree uncertainty consistently represents the smallest

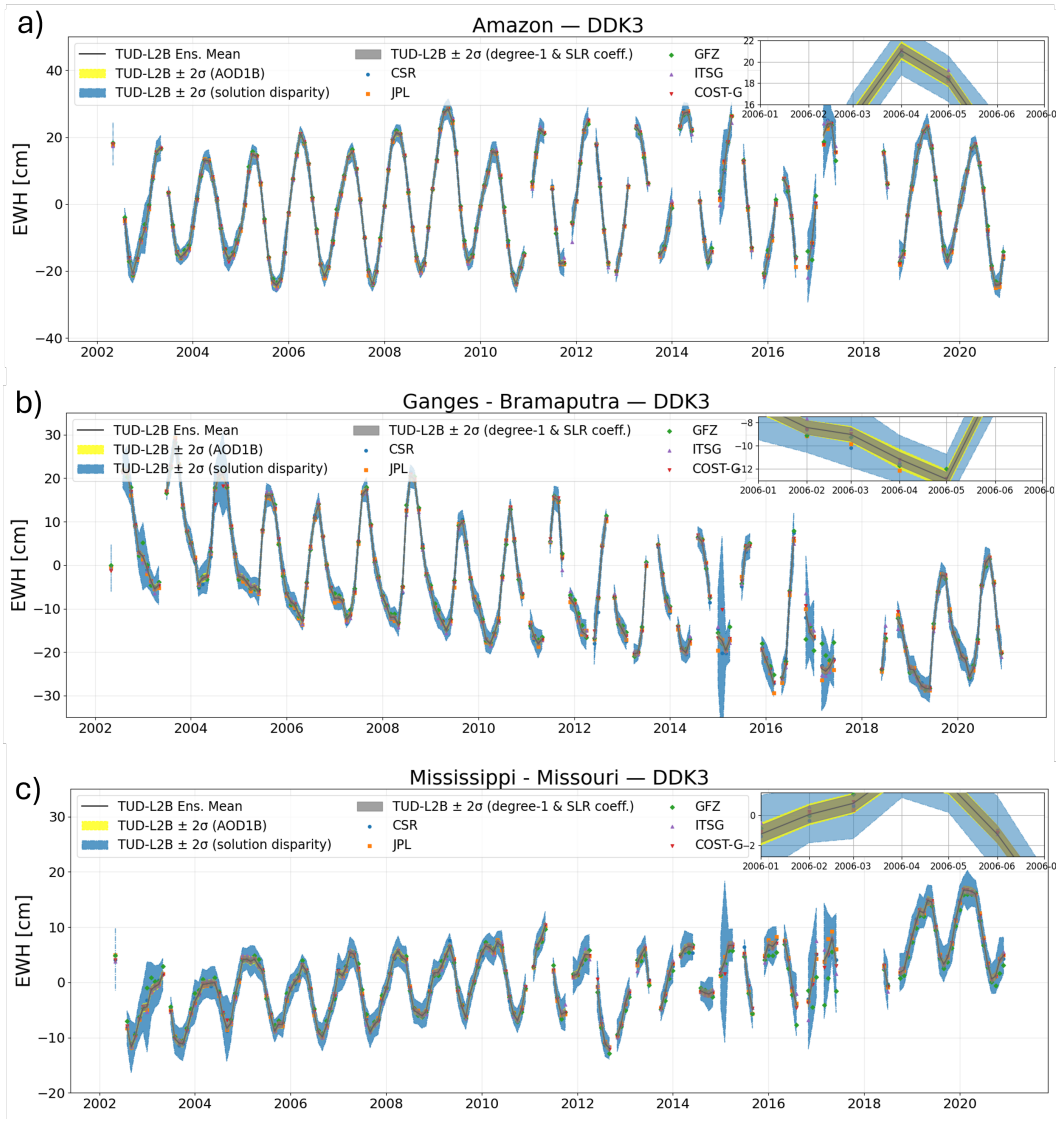

Figure 8: Basin-averaged equivalent water height (EWH) time series for three major river basins: the Amazon, Ganges–Brahmaputra, and Mississippi, derived from selected individual Level-2B GRACE/GRACE-FO DDK3-filtered-solutions (CSR, JPL, GFZ, ITSG, and COST-G) and compared with the TUD-L2B ensemble mean (for degree/order 1 to 60). Shaded envelopes indicate the ensemble uncertainty, representing the spread among contributing solutions, quantified by the 2σ standard deviation, and uncertainties related to AOD1B, and the low-degree (SLR) coefficients combined uncertainty.

contribution ($\sim$ 0.43-8%) for both ice sheets. Temporal statistics of these uncertainty components, summarised in Appendix D.2 (Table 12).

5.2.5 Ocean circulation studies

Oceanic mass variability exhibits low signal-to-noise ratios (compared to hydrological and glaciological signals) and is strongly influenced by background model errors, particularly in ocean tide and de-aliasing corrections. As a representative case study for ocean circulation processes, we examine mass variability in the Argentine Basin, with a focus on the Zapiola Rise (Figure 3). This region is well known in the context of the GRACE(-FO) mission for its sensitivity to temporally varying ocean circulation [Volkov and Fu, 2008, Yu et al., 2018, Ghobadi-Far et al., 2022, Cuadrat-Grzybowski et al., 2025].

Figure 9: Land-averaged equivalent water height (EWH) time series for (a) Antarctica and (b) Greenland, derived from selected individual Level-2B GRACE/GRACE-FO DDK3-filtered solutions (CSR, JPL, GFZ, ITSG, and COST-G) and compared with the TUD-L2B ensemble mean (degree and order 2–60). Shaded envelopes indicate $\pm 2\sigma$ (95%) uncertainty contributions associated with ensemble uncertainty, AOD1B de-aliasing, and the combined low-degree (degree-1 and SLR) uncertainty.

Area-averaged time series from Level-2B solutions are compared to the TUD-L2B ensemble mean (with all applied post-processing corrections) in Figure 10a, together with all considered uncertainty components expressed as $\pm 2\sigma$ (95%) intervals. The temporal Root-Median-Square (RMedS) of the ensemble mean signal (Figure 10b) and of the individual uncertainty contributions (Figure 10c–e) provides a complementary spatial perspective on the oceanic signal-to-noise characteristics.

The characteristic dipole mass variability associated with the Zapiola Rise is clearly identifiable in both the temporal and spatial diagnostics. In the basin-averaged time series (Figure 10a), the signal exhibits a pronounced cyclical behaviour with an amplitude of approximately 2.5 cm EWH. The corresponding spatial signature is evident in the RMedS of the ensemble mean signal (Figure 10b), which reveals a well-defined dipolar structure centred on the Zapiola Rise, with local magnitudes reaching approximately 3–5 cm.

In terms of uncertainty contributions, the ensemble uncertainty constitutes the largest component in this region. As shown by the time series envelopes and the RMedS distribution (Figure 10d), the 95% ensemble uncertainty reaches typical magnitudes of approximately 2.0–2.8 cm. This component primarily reflects residual noise and differences in background modelling choices, including ocean tide representations, among the contributing Level-2B solutions. The AOD1B-related uncertainty is of comparable magnitude and forms the second largest contribution, with 95% confidence levels of approximately 1.4–2.2 cm (Figure 10c). These uncertainties are spatially concentrated near coastal regions and leak into the Zapiola Rise area, underscoring the sensitivity of oceanic mass estimates to imperfect de-aliasing of high-frequency atmosphere–ocean variability.

The combined uncertainty associated with SLR-based low-degree coefficients and degree-1 (geocentre) corrections is substantially smaller. As shown in Figure 10e, this contribution has a basin-averaged 95% uncertainty level with a temporal mean of approximately 0.5 cm, making it the least significant uncertainty source in this region.

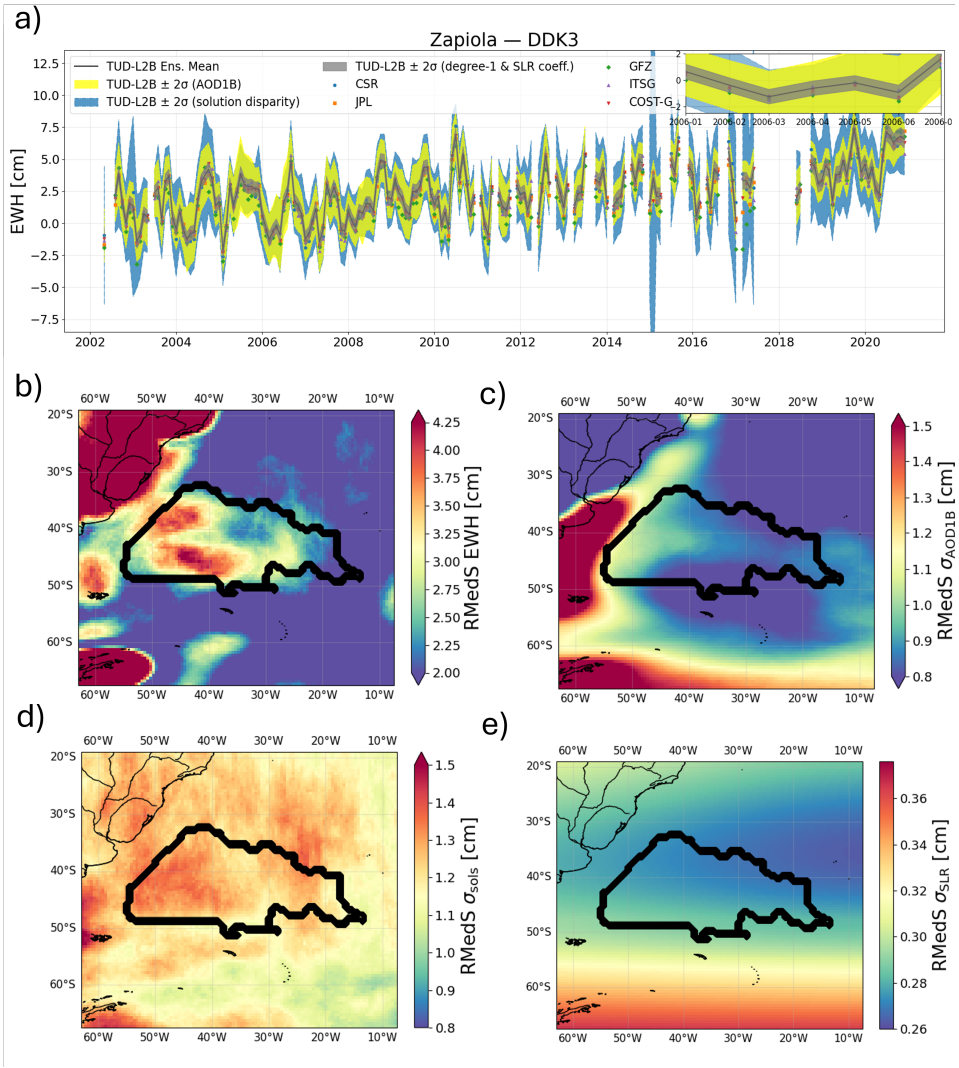

Figure 10: Equivalent water height (EWH) results for the Argentine Basin (DDK3 filtered, degree/order 2–60). (a) Basin-averaged EWH time series derived from selected Level-2B GRACE/GRACE-FO solutions (CSR, JPL, GFZ, ITSG, and COST-G), shown together with the TUD-L2B ensemble mean. Shaded envelopes denote $\pm 2\sigma$ (95%) uncertainty contributions associated with ensemble solution uncertainty, AOD1B de-aliasing, and combined SLR and degree-1 corrections. The temporal Root-Median-Square (RMedS) of 1σ fields of (b) the corrected TUD-L2B ensemble mean EWH signal ($\sim$ 3 cm), (c) the AOD1B uncertainty component ($\sim$ 0.7 cm), (d) the ensemble uncertainty ($\sim$ 1.2 cm), and (e) the low-degree SLR and degree-1 combined uncertainty ($\sim$ 0.26 cm) are also shown. Values given in parentheses denote the regional averages.

5.2.6 Leakage correction uncertainties

Leakage induced by spatial filtering is particularly pronounced in regions characterised by large signal amplitudes and sharp spatial mass variability. While decorrelation filtering substantially reduces north-south striping noise in GRACE(FO) solutions, it also attenuates true geophysical signals and redistributes signal power across basin boundaries. The DDK3 filter is widely used in hydrological applications as a compromise between noise reduction and spatial resolution. For this reason, the following analysis focuses on the leakage correction and its associated uncertainty

for DDK3 filtered solutions, although leakage corrections for the full range of DDK filters (DDK2–DDK7) are also provided in the dataset.

The spatial characteristics of the leakage correction are first examined using climatological model fits, following the approach of Section 3.4.3 [Dobslaw et al., 2020]. Figure 11 shows the climatological leakage correction expressed in terms of its linear trend, bias, and acceleration (Figure 11a–c), as well as its seasonal components. The annual leakage signal is represented by the cosine, sine, and amplitude terms (Figure 11d–f, respectively), while the semiannual leakage signal is shown analogously in Figure 11g–i respectively. The seasonal leakage amplitudes are spatially highly localised, with elevated values concentrated along regions of strong hydrological variability. In addition, pronounced leakage patterns are observed along coastal zones, reflecting land–ocean signal leakage in regions with strong land–sea mass contrasts. In the polar regions, these effects are most evident in the trend and acceleration terms, consistent with the patterns reported by Dobslaw et al. [2020]. In contrast, the seasonal leakage signals are concentrated along the coastlines of mid-latitude Africa, and much of the South American continent, with elevated amplitudes also observed along western North America, particularly in the sine components (Figure 11e and h) of the annual and semiannual terms. The bias term in particular largely reflects scaled noise introduced by the DDK4-filtered solution used in the leakage pair construction, which is evident from the pronounced north–south striping visible in Figure 11b.

The basin-scale impact of leakage correction is illustrated in Figure 12, showing basin-averaged leakage correction and uncertainty (see Section 3.4.3) time series for the Ganges–Brahmaputra, Mississippi–Missouri, and Amazon basins. We use a $\pm 1\sigma$ range for visual clarity, as the corresponding $\pm 2\sigma$ envelope would obscure the leakage correction time series. For the Ganges–Brahmaputra basin, the leakage correction exhibits a clear seasonal signal with a basin-mean amplitude of approximately 3.25 cm and a linear trend of about -0.63 cm yr^{-1} (Figure 12b). However, this signal is accompanied by a large mean leakage uncertainty of approximately 9.7 cm, which substantially exceeds both the seasonal amplitude and the long-term trend. A similar behaviour is observed for the Mississippi–Missouri basin, where a localised leakage correction trend of approximately -0.18 cm yr^{-1} is present in the basin-averaged time series (Figure 12c), while the associated mean leakage uncertainty remains high at about 8.3 cm. The basin-averaged behaviour discussed above is supported by the temporal statistics of the leakage correction uncertainty summarised in Appendix D.1.2. These statistics confirm that, for all three hydrological basins, leakage uncertainty substantially exceeds the magnitude of the basin-mean leakage correction itself, despite strong spatial cancellation in the averaged signal. For completeness, analogous leakage uncertainty statistics for the polar regions are provided in Appendix D.2.2. For the Amazon basin, the leakage climatological signal shows substantially larger annual and semiannual amplitudes within the basin, reaching approximately 20 cm and 4 cm, respectively, as evident from the spatial amplitude maps in Figure 11f and i. These amplitudes are highly localised and are characterised by alternating positive and negative anomalies across the basin. When averaged over the full basin area, these opposing contributions largely cancel, resulting in a basin-mean leakage correction that remains bounded within approximately ± 2 cm in the time series (Figure 12a). Despite this small basin-mean leakage correction for the Amazon, the basin-averaged leakage uncertainty inferred from the time series has a temporal mean of approximately 9.8 cm. This indicates that strong spatial averaging substantially reduces the apparent magnitude of the leakage correction while leaving the associated uncertainty largely unaffected. Consequently, basin-averaged leakage corrections may appear small even in the presence of pronounced local leakage signals visible in the spatial climatologies, and their interpretation therefore requires caution in basin-scale analyses, particularly when sub-basin or regional processes are of interest.

5.3 Global Spatial Distribution of Signal and Uncertainties

To complement the application-specific analyses, we compute the temporal RMS of the DDK3-filtered Level-2B solutions at each grid cell and present the global results in Figure 13. Panels (a) and (b) show the RMS of the ensemble-mean EWH signal and the ensemble solution uncertainty, respectively. Panels (c) and (d) display the RMS of the climatologically reconstructed signal and its residuals, noting that the reconstruction does not include aliasing tidal constituents (S2, P1, S1, K1, and R3). Panels (e) and (f) illustrate the combined SLR-derived and degree-1 contribution and its associated uncertainty, while panels (g) and (h) present the leakage correction and its associated uncertainty.

The ensemble mean signal RMS (Figure 13a) has a global mean of 6.34 cm, representing the magnitude of temporal mass variability resolved by GRACE and GRACE FO. The climatologically reconstructed signal (Figure 13c) shows a slightly smaller global mean RMS of 5.64 cm. This confirms that the fitted climatological model captures most ($\sim 88\%$) of the temporal variability. The remaining difference reflects contributions not represented by the climatology, including noise, particularly visible over the oceans in Figure 13a, as well as episodic or extreme events that deviate from the assumed climatological function. For reference, when the aliasing tidal constituents S2, P1, S1, K1, and R3 (see Section B.4) are included in the reconstruction, the global mean temporal RMS amounts to 5.72 cm (90%). This implies that unresolved tidal aliasing accounts for approximately 0.08 cm (or $1-2\%$) of the total RMS difference between the ensemble mean signal and the climatological reconstruction. The remaining discrepancy is therefore primarily

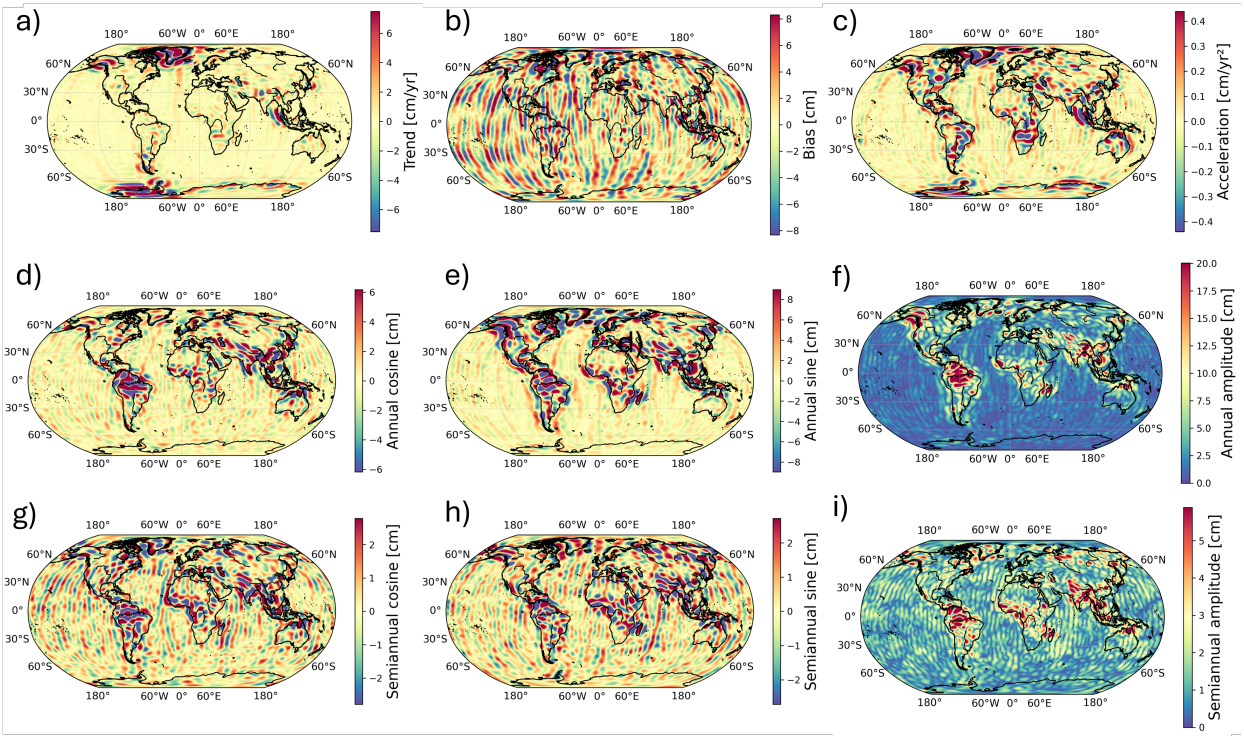

Figure 11: Climatological fitted parameters (referenced to epoch 2008.0) of the leakage correction derived following the method of Dobslaw et al. [2020], based on DDK3 filtered Level-2B solutions (degree and order 2–60). Shown are (a) linear trend, (b) bias, and (c) acceleration of the leakage correction model. The annual leakage signal is represented by (d) cosine, (e) sine, and (f) amplitude term, while the semiannual leakage signal is shown by (g) cosine, (h) sine, and (i) amplitude term.

attributable to residual noise and non-climatological variability which can observed in Figure 13d. The remaining discrepancy is therefore primarily attributable to residual noise and non-climatological variability, as illustrated in Figure 13d, which shows a global mean RMS of 2.22 cm. Elevated values are observed in regions of strong hydrological variability, such as the Amazon, central Africa, Mississippi, and Ganges–Brahmaputra basins, as well as over Greenland and Antarctica, where they are associated with pronounced melt events (e.g. the summer of 2012; Velicogna et al., 2014).

Among the uncertainty components, the ensemble uncertainty RMS (Figure 13b) reaches a global mean of 1.71 cm, representing the dominant global uncertainty source in this comparison. Spatially, remnants of north–south striping are still visible, with local magnitudes exceeding 3 cm. Elevated values are also apparent in regions where background ocean tide models differ more strongly between processing centres, for example along the western coast of Antarctica (up to $\sim$ 3 cm) and along the western and northern coasts of Australia ($\sim$ 2 cm). Away from these regions, ensemble uncertainty values tend to be closer to the global mean.

The combined SLR-derived and degree-1 contribution (Figure 13e) exhibits a global mean RMS of 1.96 cm. Spatially, the signal is predominantly concentrated in the Northern Hemisphere, where local RMS values reach approximately 5 cm, but notable contributions are also present in the Southern Hemisphere, with amplitudes of around 2.5 cm. The uncertainty associated with this combined component (Figure 13f) is comparatively small, with a global mean RMS of only 0.38 cm. As expected, higher uncertainties are observed in both polar regions (0.4–0.6 cm), and faint zonal (latitude-aligned) stripes are visible, reflecting the residual low-degree structure from the former $C_{2,0}$ and $C_{3,0}$ coefficients. In these stripes, uncertainties vary locally, with values around 0.2 cm in the low-uncertainty bands and increasing to 0.4 cm between them.

The leakage correction (Figure 13g) exhibits a global mean RMS of 16.27 cm, highlighting its substantial magnitude relative to the DDK3-filtered signal (approximately 2.5–3 times larger). Highly localised signals, with amplitudes ranging from 15 cm to over 25 cm, are observed in regions of strong variability, including land hydrology hotspots, the central Greenland ice sheet (see the central leakage anomaly), and coastal regions worldwide.

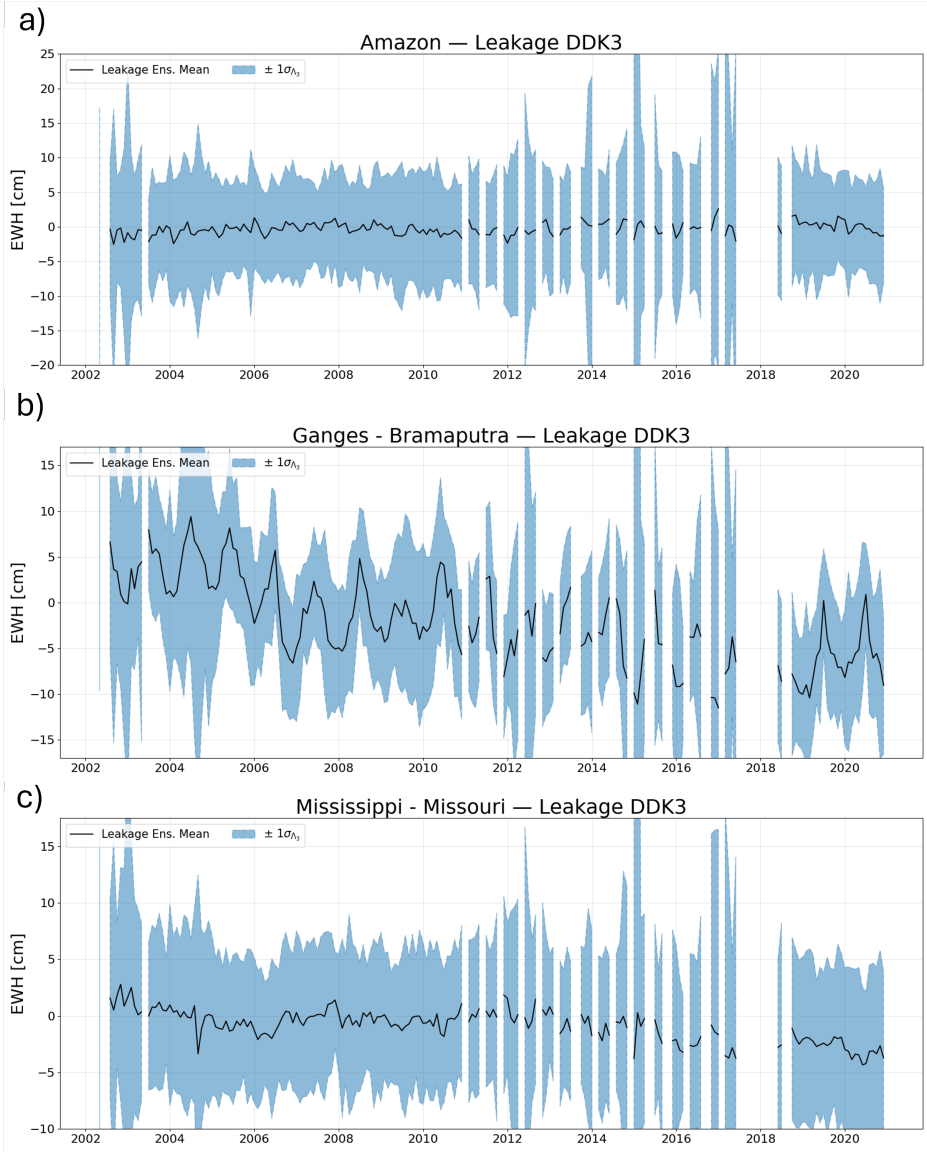

Figure 12: Basin averaged leakage correction using the method by Dobslaw et al. [2020] time series for major river basins based on DDK3 filtered Level-2 solutions (degree and order 2–60): (a) Amazon, (b) Ganges–Brahmaputra, and (c) Mississippi–Missouri. Shown are the basin mean leakage correction signals together with their associated uncertainty envelopes as $\pm 1\sigma$. A 1σ representation is used here for visual clarity, as the corresponding 2σ envelopes would obscure the leakage correction signal.

The associated uncertainty of the leakage correction (Figure 13h) is also significant, with a global mean RMS of 10.07 cm. Spatially, it resembles the ensemble solution uncertainty (Figure 13b), exhibiting pronounced north–south stripes with values of 7–15 cm, but it also shows elevated uncertainty in the western Antarctic coast (10–15 cm) and the interior of Greenland (approximately 10–12 cm). The magnitude and spatial patterns of both the leakage correction and its uncertainty underline the need for caution when interpreting these fields in quantitative analyses.

Overall, the global RMS diagnostics confirm that, at the global scale, the ensemble uncertainty constitutes the largest structured uncertainty component, followed by AOD1B (see Figure 6 in Section 5.2.1), and the combined SLR-based and degree-1 uncertainties contribute at the sub-centimetre level.

In this paper, we present the construction and release of **TUD-L2B-EWH_UNC-GRACE**, a globally gridded Level-2B GRACE and GRACE-FO equivalent water height (EWH) dataset with explicitly quantified uncertainty components. The

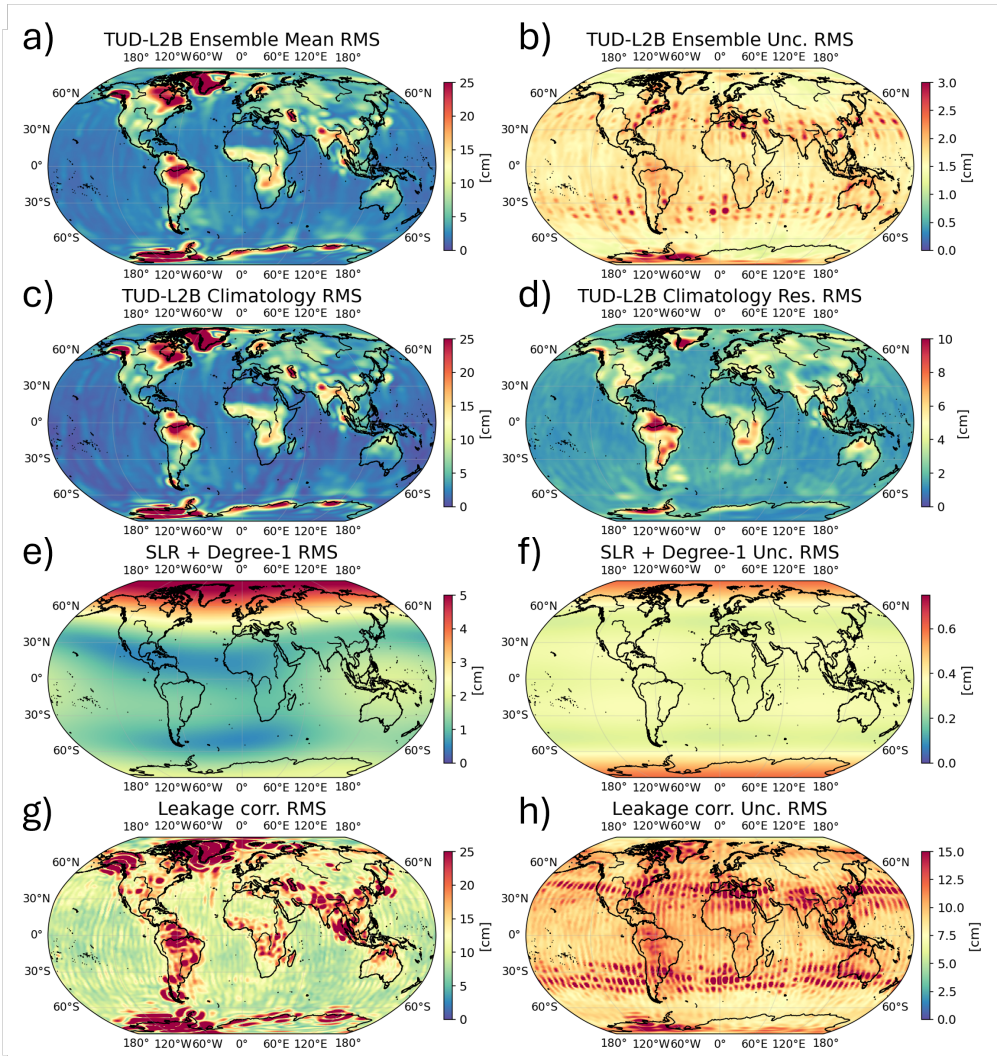

Figure 13: Global distribution of temporal RMS derived from DDK3-filtered Level-2B solutions (degree/order 2–60). Panels show the RMS of (a) the ensemble-mean EWH signal (global mean RMS: 6.34 cm), (b) the ensemble solution uncertainty (see Figure 13b), (c) the climatologically reconstructed EWH signal (5.64 cm), (d) the climatological residuals (2.22 cm), (e) the combined SLR-derived and degree-1 contribution (1.96 cm), (f) its associated uncertainty (0.38 cm), (g) the leakage correction (16.27 cm), and (h) its associated uncertainty (10.07 cm). Values in parentheses indicate the global mean RMS for each panel. All values are expressed in centimetres of equivalent water height (cm EWH).

dataset preserves the original Level-2B mass anomaly content and provides separate gridded estimates of uncertainty arising from differences between processing centres, background model errors, low-degree coefficient replacement, filtering, and Glacial Isostatic Adjustment (GIA) modelling. The ensemble-mean signal and the associated ensemble uncertainty are computed using time-dependent weights based on the inverse squared open-ocean RMS of each solution. This weighting scheme reduces the influence of noisier solutions and minimises the overall noise level in the combined product.

A central feature of the product is the explicit separation of individual uncertainty components, provided in gridded form and for multiple DDK filter levels. This enables users to assess how different error sources contribute to the total uncertainty at basin, regional, or grid scale, and to construct application-specific uncertainty estimates rather than relying on a single aggregated error metric. Notwithstanding, we also provide the aggregate uncertainty and the ensemble mean corrected for C2,0 and C3,0 from SLR, geocenter motion, GIA ensemble mean, and ocean tidal aliasing, ready to be used directly. This is particularly relevant for hydrological data assimilation studies, where spatially resolved observation error estimates are required to properly weight GRACE-derived mass anomalies within land surface or

groundwater models. The consistency and practical relevance of this framework are demonstrated through representative applications in hydrology, glaciology, and ocean circulation, where the relative importance of the different uncertainty components is evaluated in realistic use cases.

In addition to the main uncertainty product, several ancillary datasets are provided. These include **TUD-L2B-EWH_UNC-GRACE_noSLR**, in which low-degree coefficients are not replaced by satellite laser ranging (SLR) solutions, as well as climatological products describing fitted signal and leakage components, released as **TUD-L2B-EWH_CLIM-GRACE**, **TUD-L2B-EWH_CLIM_CORR-GRACE** and **TUD-L2B-EWH_CLIM_LEAKAGE-GRACE**. Together, these ancillary products support sensitivity analyses of low-degree replacement using SLR, climatological fitting, and leakage correction.

Rather than prescribing a single error model, **TUD-L2B-EWH_UNC-GRACE** is designed to make the transition from Level-2 spherical harmonic solutions to Level-2B gridded EWH fields explicit in terms of uncertainty. The dataset exposes how individual error sources propagate at the Level-2B stage. In this way, it provides a transparent bridge between monthly spherical harmonic coefficients and geophysical applications that require spatially resolved, traceable uncertainty information.

Data Availability

The **TUD-L2B-EWH_UNC-GRACE** dataset is publicly available at `http://doi.org/10.4121/4fc748e8-01c7-4f06-87da-653937b078f7` in CF-compliant NetCDF format, and is also distributed through the TUDelft GRACE-Cube portal (`https://grace-cube.lr.tudelft.nl/`). A simple Python script is provided in the accompanying README file to facilitate opening the NetCDF files, reconstructing the climatological signal, and optionally removing tidal aliasing components.

A Level-2B residuals distribution

To assess the validity of using the (weighted) standard deviation as an estimator of solution uncertainty, we analyze the distribution of residuals of each Level-2B solution with respect to the ensemble mean. For each solution, residual values are aggregated over all spatial grid points to form a single empirical distribution, shown in Figure 14. We provide for these distributions in Table 7, three summarising statistics: median, inter-quartile range (IQR), and standard deviation.

Table 7: Statistical properties (median, inter-quartile range, and standard deviation) of ravelled residual distributions. All values are given in cm.

Solution	Median [cm]	IQR [cm]	Std. dev. [cm]
ITSG	0.028	2.520	2.577
CSR	0.007	3.114	2.773
JPL	0.011	3.057	2.933
TONGJI	0.024	3.178	3.153
HUST	-0.014	3.527	3.170
GFZ	-0.087	3.505	3.400
APM-SYSU	0.022	3.240	5.977

Across all solutions, median residuals are of order 10^{-2} cm (Table 7), indicating negligible systematic bias relative to the ensemble mean. The IQR values are comparable among most solutions and closely reflect the distribution widths seen in Figure 14, with ITSG exhibiting the narrowest spread and GFZ and HUST showing slightly broader cores.

APM-SYSU displays a markedly larger standard deviation, despite an IQR comparable to the other solutions. This behaviour is consistent with strong outlier sensitivity, which is attributed to orbit repeat patterns (see Section 3.3).

Overall, the close correspondence between Figure 14 and the statistics in Table 7 supports the use of the (weighted) standard deviation of residuals as a quantitative measure of the ensemble uncertainty.

B Aliasing period

We summarise the standard formulation used to compute tidal aliasing periods in the context of GRACE(-FO) observations. The material is included for completeness and to document auxiliary calculations used in this study; it does not introduce any methodological novelty.

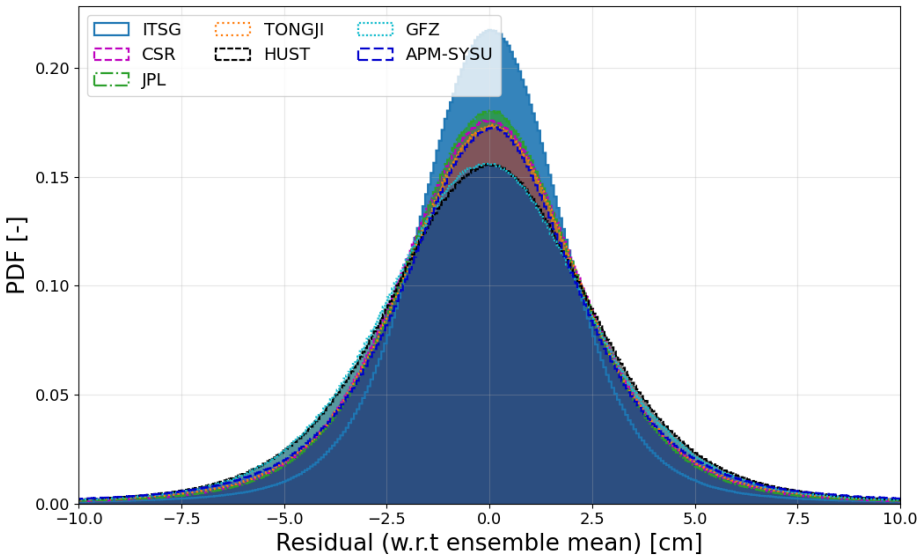

Figure 14: Distributions of equivalent water height (EWH) residuals (in cm) relative to the ensemble mean for all Level-2B solutions (DDK4 filtered, spherical harmonic degree/order 2–60).

The aliasing frequency, f_A, of a tidal constituent with true frequency f is given by

$$f_A = |n_f f_s - f|\,, \tag{10}$$

where n_f is an integer and f_s denotes the effective GRACE(-FO) sampling frequency. Following Koch et al. [2024], the sampling frequency is defined as

$$f_s = \omega - \dot{\Omega}, \tag{11}$$

with ω the Earth's sidereal rotation rate, taken as $\omega = 360.9865\ ^\circ\,\mathrm{day}^{-1}$ (IERS 2010 convention), and $\dot{\Omega}$ the nodal precession rate of the satellite orbit.

B.1 Nodal precession rate

The nodal precession rate is not strictly constant in time, as it depends on several slowly varying orbital and geophysical parameters. To first order, it is approximated by

$$\dot{\Omega}(t) \approx -\frac{3}{2}\, J_2(t) \left(\frac{R}{R + h(t)}\right)^2 n(t)\, \cos(i(t))\,, \tag{12}$$

where J_2 is the Earth's oblateness coefficient, related to the degree-2 zonal Stokes coefficient by $J_2 = -\sqrt{5}\, C_{2,0}$. Here, R denotes the mean Earth radius, $h(t)$ the satellite mean altitude, $i(t)$ the orbital inclination, and $n(t)$ the mean motion (the latter three are functions of time).

B.2 Time-varying orbital elements

In many GRACE-related studies, $\dot{\Omega}$ is treated as a constant, typically within the range -0.132 to $-0.136\ ^\circ, \mathrm{day}^{-1}$ [Ray and Luthcke, 2006, Liu and Sneeuw, 2021, Li et al., 2022, Koch et al., 2024]. To verify the consistency of this commonly adopted range, we explicitly recomputed $\dot{\Omega}(t)$ by accounting for the temporal variability of $h(t)$, $i(t)$, and $J_2(t)$. Monthly mean values were used for the satellite altitude and inclination, while monthly estimates of J_2 were derived from SLR solutions [Loomis et al., 2020]. Although the resulting temporal variations in $\dot{\Omega}$ are small ($\sim 3\%$), they lead to non-negligible differences in aliasing period estimates, ranging from 0.1% up to approximately 5% (e.g. K_1 tide), highlighting the sensitivity of aliasing periods to the assumed nodal precession rate.

The resulting time series of the relevant input parameters is shown in Figure 15. These calculations are included solely to verify the validity of the nodal precession rates commonly assumed in aliasing analyses. The temporal variability of J_2 reflects the well-known SLR-derived $C_{2,0}$ variations, which are of order 10^{-10}. Over the mission lifetime, the satellites'

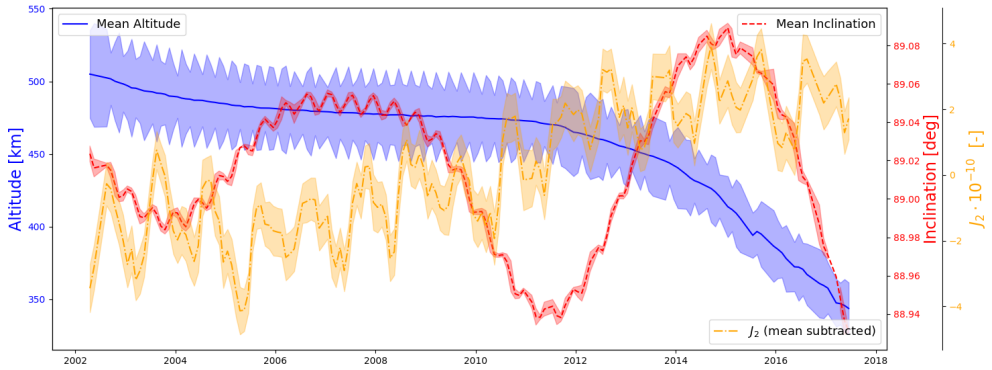

Figure 15: Monthly mean GRACE satellite altitude and inclination from April 2002 to June 2017, together with the corresponding mean-subtracted J_2 estimates derived from Satellite Laser Ranging (SLR) [Loomis et al., 2020]. Shaded regions indicate the $\pm 1\sigma$ uncertainty bounds: for altitude and inclination, these correspond to the intra-monthly standard deviations, while for J_2 they represent the formal errors of the SLR-derived $C_{2,0}$ estimates.

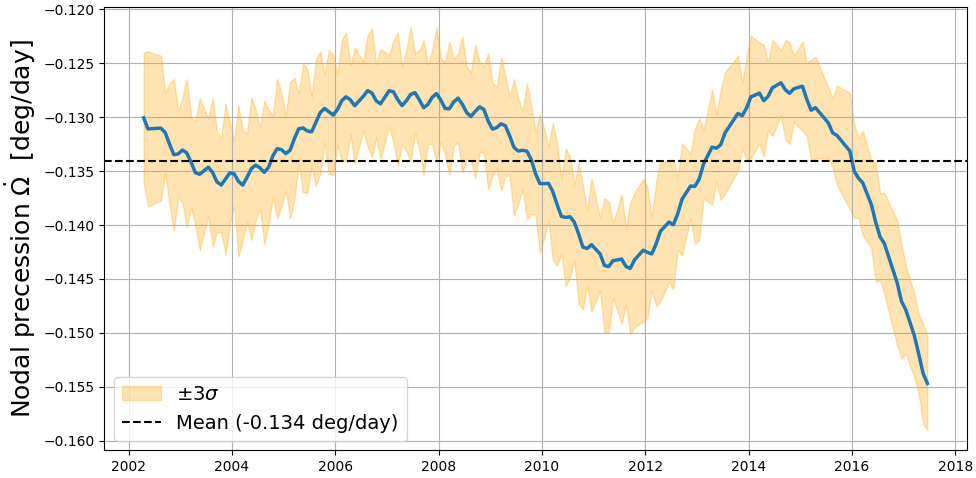

Figure 16: Time series of the GRACE nodal precession rate $\dot{\Omega}$ computed from time-varying altitude, inclination, and J_2, including $\pm 3\sigma$ uncertainty bounds.

mean altitude decreases from approximately 500 km in April 2002 to about 350 km by June 2017, shortly before re-entry. The inclination exhibits only small oscillatory variations, with a peak-to-peak amplitude of approximately $0.18°$ around an expected mean value of $\sim 89.02°$.

B.3 Resulting nodal precession rate variability

Using the time-varying orbital elements and oblateness factors described above, we computed the full time series of the nodal precession rate $\dot{\Omega}(t)$ over the GRACE mission lifetime. The resulting evolution is shown in Figure 16, including $\pm 3\sigma$ uncertainty bounds propagated from the monthly uncertainties in altitude, inclination, and J_2. Note that, unlike the less conservative $\pm 2\sigma$ bounds used throughout the main text, the wider $\pm 3\sigma$ envelope is adopted here to capture even small variations in $\dot{\Omega}(t)$, which, due to the high sensitivity of tidal aliasing periods to the nodal precession rate, can have a disproportionately large influence on the resulting alias frequencies.

The nodal precession rate varies approximately periodically throughout the mission, primarily driven by long-term orbital decay, with secondary contributions from variations in inclination and, to a lesser extent, from changes in J_2. Over the period from April 2002 to June 2017, $\dot{\Omega}$ ranges from approximately $-0.130\ ^\circ\,\mathrm{day}^{-1}$ in the early mission phase to about $-0.155\ ^\circ\,\mathrm{day}^{-1}$ toward the end of the mission, as the satellites approached re-entry. The time-averaged nodal precession rate is $-0.134\ ^\circ\,\mathrm{day}^{-1}$, with a temporal standard deviation of $0.005869\ ^\circ\,\mathrm{day}^{-1}$.

These results confirm that the commonly adopted constant values of $\dot{\Omega}$ used in GRACE aliasing analyses lie well within the mission-mean range. In light of this consistency, we adopt a representative constant value of $\dot{\Omega} = -0.134\,^{\circ}\mathrm{day}^{-1}$ for the aliasing calculations presented in this study.

B.4 Resulting tidal amplitudes

Following the estimation of the nodal precession rate ($\dot{\Omega}$), we analyse the resulting tidal aliasing amplitudes. Figure 17 presents the spatial distribution of the aliased signals for the main tidal constituents, namely (a) S_2, (b) S_1, (c) P_1, (d) K_1, and the unmodelled component (e) R_3 discussed in Section 3.2.

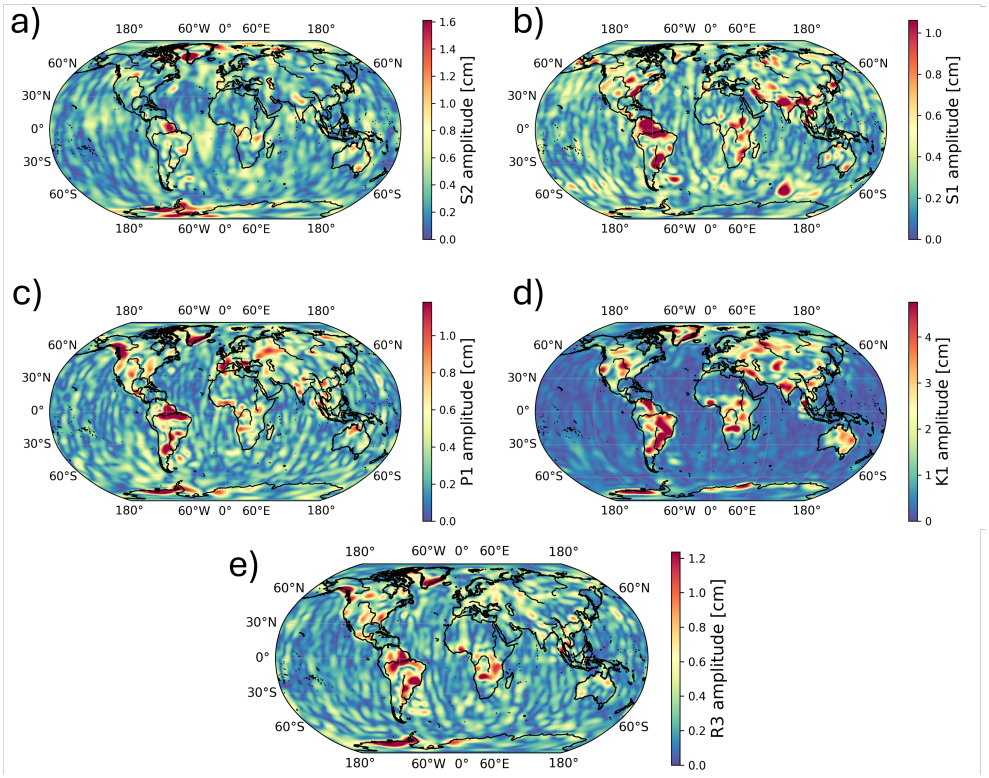

Figure 17: Spatial distribution of tidal aliasing amplitudes derived from a nodal precession rate, $\dot{\Omega} = -0.134\,^{\circ}\,\mathrm{day}^{-1}$, and the DDK3-filtered TUD-L2B Ensemble mean, for the main constituents: (a) S2, (b) S1, (c) P1, (d) K1, and (e) unmodelled R3. Amplitudes are expressed in centimetres equivalent water height (cm EWH).

Maximum amplitudes reach approximately 1.6 cm (S_2), 1.25 cm (P_1), 1.0 cm (S_1), 4.5 cm (K_1), and 1.25 cm (R_3). The spatial patterns differ significantly between constituents. The S_2 signal is predominantly concentrated over oceans and coastal regions, with pronounced amplitudes in the southwest of Greenland, coastal West Antarctica, and semi-enclosed basins such as the Caspian Sea. In contrast, $S_1$and P_1exhibit lower amplitudes but are more strongly expressed over land, with notable signals in the Amazon basin, the Indian subcontinent (India and Bangladesh), and central African river basins. For P_1, the Antarctic signal is primarily confined to West Antarctica, with little expression along the eastern coast.

The K_1 constituent shows the largest amplitudes and a distinct spatial signature, with strong signals over both continental interiors and coastal regions. In particular, amplitudes of 2–4 cm are observed along the entire Greenland coastline and 1–5 cm along the Antarctic coastline, with additional large-scale signals extending across South America, including the Argentine Basin and the Zapiola Rise region [Volkov and Fu, 2008, Han et al., 2014].

The unmodelled R3 component exhibits a spatial pattern broadly similar to S_1 and P_1, with moderate amplitudes over land and coastal regions. Enhanced values are observed in West Antarctica, southeastern Greenland, parts of South America (0.5–1.25 cm), and central Africa, with weaker signatures also present in the Zapiola Rise.

Overall, S_2 is primarily oceanic and coastal, whereas $S_1$and P_1 are characterised by lower-amplitude signals over land. K_1 dominates both land and coastal regions with substantially larger amplitudes. All constituents show some degree of aliasing of the dipolar signal associated with the Zapiola Rise, particularly for S_1, P_1, and R_3.

C Overview of variable composition and low-degree content

This appendix summarises the geophysical content of the variables provided in the `TUD-L2B-EWH_UNC-GRACE` data product and its ancillary variant `TUD-L2B-EWH_UNC-GRACEnoSLR`. Tables 8 and 9 indicate which spherical harmonic components are included in each variable, explicitly distinguishing between degree-1 (geocenter), the low-degree coefficients $C_{2,0}$ and $C_{3,0}$, and all remaining degrees (2–60).

Table 8: Overview of geophysical components represented in the variables of the `TUD-L2B-EWH_UNC-GRACE` product. Checkmarks indicate that the corresponding contribution is included in the variable. Entries marked "SLR" indicate that the coefficient is replaced by Satellite Laser Ranging solutions following TN-14v3. Degree-1 (geocenter) contributions are provided explicitly and are not included by default in other variables. "All other" refers to spherical harmonic degrees 2–60 excluding degree-1, $C_{2,0}$, and $C_{3,0}$.

Variable	Degree-1	$C_{2,0}$	$C_{3,0}$	All other
`ewh_mean`	No	SLR	SLR	Yes
`ewh_mean_corr`	Yes	SLR	SLR	Yes
`ewh_unc_sols`	No	SLR	SLR	Yes
`ewh_unc_degree20`	No	Yes	No	No
`ewh_unc_degree30`	No	No	Yes	No
`ewh_unc_aod1b`	No	Yes	Yes	Yes
`ewh_degree1`	Yes	No	No	No
`ewh_unc_degree1`	Yes	No	No	No
`ewh_gia_mean`	No	Yes	Yes	Yes
`ewh_gia_unc`	No	Yes	Yes	Yes
`ewh_mean_leakage`	No	SLR	SLR	Yes
`ewh_unc_leakage`	No	SLR	SLR	Yes

Table 9: Overview of geophysical components represented in the variables of the `TUD-L2B-EWH_UNC-GRACEnoSLR` ancillary product. In this product, low-degree coefficients $C_{2,0}$ and $C_{3,0}$ are *not* replaced by SLR solutions. Degree-1 (geocenter) contributions are not included. "All other" refers to spherical harmonic degrees 2–60 excluding degree-1, $C_{2,0}$, and $C_{3,0}$.

Variable	Degree-1	$C_{2,0}$	$C_{3,0}$	All other
`ewh_mean`	No	Yes	Yes	Yes
`ewh_unc_sols`	No	Yes	Yes	Yes

D Additional uncertainty statistics

D.1 Uncertainties in hydrological regions

This appendix provides basin-averaged temporal statistics of uncertainty components affecting GRACE(-FO) equivalent water height (EWH) time series over major hydrological basins. All statistics are reported as 2σ values and are derived from DDK3-filtered Level-2B solutions (degree and order 2–60). The purpose of this section is to complement Section D.1.1 by providing quantitative summaries of the individual uncertainty contributions discussed therein.

D.1.1 Level-2B uncertainty components

Table 10 summarises the dominant Level-2B uncertainty components for the Amazon, Mississippi–Missouri, and Ganges–Brahmaputra basins. Across all three basins, AOD1B-related uncertainty is approximately 0.6–0.8 cm EWH and standard deviations below 0.10 cm, indicating that residual atmosphere–ocean de-aliasing errors are a minor contribution at the basin scale. The ensemble uncertainty is consistently larger, with mean values of about 2.6–3.2 cm and standard deviations of roughly 1.4–2.0 cm, reflecting differences among Level-2B processing strategies and background models.

Uncertainties associated with low-degree coefficients, including degree-1 (geocentre motion), SLR-derived $C_{2,0}$ and $C_{3,0}$, and their combined contribution, are smaller by one order of magnitude (i.e. from 0.6 to 1.0 cm) compared to ensemble uncertainty and similar in magnitude to the AOD1B uncertainty, but remain non-zero and are therefore retained for completeness. The very large maximum values occasionally observed for the ensemble uncertainty are primarily associated with unfavourable orbit repeat patterns and sampling geometry, rather than representative basin-scale variability.

Table 10: Basin-averaged 2σ uncertainty statistics for major river basins derived from Level-2B GRACE(-FO) solutions (DDK3 filtered, degree/order 2–60). Shown are descriptive statistics of solution-based ensemble uncertainty, AOD1B de-aliasing uncertainty, degree-1 (geocentre), SLR-derived low-degree coefficients, and their combined uncertainty. All values are given in centimetres equivalent water height.

Basin	Uncertainty source	Mean	Median	Std. dev.	Min	Max
Amazon	Ensemble uncertainty	3.14	2.76	1.50	1.74	11.70
	AOD1B uncertainty	0.80	0.80	0.08	0.60	1.08
	Degree-1 uncertainty	0.58	0.58	0.00	0.58	0.58
	SLR $C_{2,0}$ uncertainty	0.28	0.28	0.02	0.22	0.34
	SLR $C_{3,0}$ uncertainty	0.10	0.00	0.12	0.00	0.32
	Combined SLR + degree-1	0.66	0.64	0.04	0.62	0.76
Mississippi–Missouri	Ensemble uncertainty	2.72	2.34	1.44	1.40	13.42
	AOD1B uncertainty	0.66	0.66	0.06	0.50	0.80
	Degree-1 uncertainty	0.56	0.56	0.00	0.56	0.56
	SLR $C_{2,0}$ uncertainty	0.08	0.08	0.00	0.06	0.10
	SLR $C_{3,0}$ uncertainty	0.16	0.00	0.18	0.00	0.52
	Combined SLR + degree-1	0.62	0.58	0.06	0.56	0.80
Ganges–Brahmaputra	Ensemble uncertainty	2.94	2.46	2.00	1.44	22.02
	AOD1B uncertainty	0.66	0.66	0.10	0.46	0.96
	Degree-1 uncertainty	0.58	0.58	0.00	0.58	0.58
	SLR $C_{2,0}$ uncertainty	0.12	0.12	0.02	0.10	0.14
	SLR $C_{3,0}$ uncertainty	0.24	0.00	0.30	0.00	0.84
	Combined SLR + degree-1	0.70	0.58	0.14	0.58	1.02

D.1.2 Leakage correction uncertainty

For completeness, Table 11 reports basin-averaged statistics of the leakage correction uncertainty. Leakage is shown separately from the Level-2B uncertainty components, as it arises from post-processing choices related to spatial filtering and is treated independently in the main analysis. All values represent 2σ temporal statistics of basin-averaged leakage uncertainty.

The leakage uncertainties reported here are one to two orders of magnitude larger than the filtered signal uncertainty components discussed in Section D.1.1, reflecting the dominant role of spatial filtering in the overall error budget. The extremely large maximum values are attributed to resonance orbit periods, during which the GRACE ground-track sampling degrades significantly, amplifying leakage errors.

Table 11: Basin-averaged 2σ statistics of leakage correction uncertainty for major river basins (DDK3 filtered, degree/order 2–60). Values are given in centimetres equivalent water height (cm EWH).

Basin	Mean	Median	Std. dev.	Min	Max
Amazon	19.70	16.72	10.50	10.40	93.92
Mississippi–Missouri	16.64	14.20	11.80	8.60	150.92
Ganges–Brahmaputra	19.48	15.44	15.36	9.50	176.46

D.2 Uncertainties in glaciological regions

This appendix summarises basin-averaged temporal statistics of uncertainty components affecting GRACE(-FO) equivalent water height (EWH) time series over Greenland and Antarctica. All statistics are reported as 2σ values and are derived from DDK3-filtered Level-2B solutions (degree and order 2–60). The purpose of this section is to provide additional quantitative context to the uncertainty magnitudes discussed in the main text.

D.2.1 Level-2B uncertainty components

Table 12 summarises the dominant Level-2B uncertainty components. The ensemble uncertainty represents the largest contribution for both basins, with mean values of 2.82 cm (Greenland) and 2.60 cm (Antarctica) at the 2σ level. The variability of this component is also comparatively large, reflected in standard deviations of 1.18 cm and 1.66 cm and maximum values reaching 12.24 cm and 17.50 cm for Greenland and Antarctica, respectively.

AOD1B-related uncertainty forms the second largest contribution and is the most important systematic component after the ensemble spread. Mean 2σ values amount to 1.40 cm for Greenland and 2.00 cm for Antarctica. Relative to the ensemble uncertainty, this corresponds to roughly 50% of the ensemble contribution for Greenland and about 77% for Antarctica. The larger influence over Antarctica reflects the stronger sensitivity of this basin-scale signal to atmospheric and oceanic mass variability represented by the AOD1B de-aliasing model. The temporal variability of this component is moderate, with standard deviations of 0.30 cm and 0.50 cm and maxima of 2.18 cm and 3.74 cm for Greenland and Antarctica, respectively.

Uncertainties associated with low-degree coefficients are substantially smaller. The degree-1 (geocentre) contribution is constant in time at approximately 0.52 cm for both basins. SLR-derived low-degree coefficients contribute mean uncertainties of about 0.52–0.56 cm for $C_{2,0}$ and 0.44–0.48 cm for $C_{3,0}$, although the latter exhibits strong skewness with medians close to zero and occasional maxima exceeding 1.4–1.6 cm. When combined with the degree-1 contribution, the resulting mean uncertainty amounts to approximately 0.98 cm for Greenland and 1.04 cm for Antarctica.

Overall, the uncertainty budget is therefore dominated by the ensemble spread and AOD1B de-aliasing errors, which together exceed the combined contribution of low-degree coefficient uncertainties by a factor of roughly two to three on average. The low-degree terms nevertheless contribute a persistent background uncertainty of order $\sim$1 cm (2σ) and are retained in the total uncertainty estimate.

Table 12: Basin-averaged 2σ uncertainty statistics for Greenland and Antarctica derived from Level-2B GRACE(-FO) solutions (DDK3 filtered, degree/order 2–60). Shown are descriptive statistics of ensemble uncertainty, AOD1B de-aliasing uncertainty, degree-1 (geocentre), SLR-derived low-degree coefficients, and their combined uncertainty. All values are given in centimetres equivalent water height (cm EWH).

Region	Uncertainty source	Mean	Median	Std. dev.	Min	Max
Greenland	Ensemble uncertainty	2.82	2.60	1.18	1.46	12.24
	AOD1B uncertainty	1.40	1.36	0.30	0.86	2.18
	Degree-1 uncertainty	0.52	0.52	0.00	0.52	0.52
	SLR $C_{2,0}$ uncertainty	0.52	0.52	0.04	0.42	0.66
	SLR $C_{3,0}$ uncertainty	0.44	0.02	0.54	0.00	1.48
	Combined SLR + degree-1	0.98	0.78	0.30	0.68	1.70
Antarctica	Ensemble uncertainty	2.60	2.24	1.66	1.72	17.50
	AOD1B uncertainty	2.00	1.90	0.50	1.24	3.74
	Degree-1 uncertainty	0.52	0.52	0.00	0.52	0.52
	SLR $C_{2,0}$ uncertainty	0.56	0.56	0.06	0.44	0.70
	SLR $C_{3,0}$ uncertainty	0.48	0.02	0.60	0.00	1.64
	Combined SLR + degree-1	1.04	0.80	0.34	0.70	1.86

D.2.2 Leakage uncertainty

For completeness, Table 13 reports basin-averaged statistics of the leakage correction uncertainty. Leakage is shown separately from the Level-2B uncertainty components, as it arises from post-processing choices related to spatial filtering and is treated independently in the main analysis. All values represent 2σ temporal statistics of basin-averaged leakage uncertainty.

The leakage uncertainties reported here are substantially larger than the filtered Level-2B uncertainty components discussed in Section D.2.1. Mean values reach approximately 21.4 cm EWH for Greenland and 16.6 cm EWH for Antarctica, with temporal standard deviations of about 8.0 cm and 9.1 cm, respectively. These values reflect the strong influence of spatial filtering and signal attenuation near coastlines and ice–ocean boundaries, which enhance leakage effects when basin averages are computed. The extremely large maximum values are attributed to resonance orbit periods, during which the GRACE ground-track sampling degrades significantly and filtering-induced leakage errors become temporarily amplified.

Table 13: Basin-averaged 2σ statistics of leakage correction uncertainty for Greenland and Antarctica (DDK3 filtered, degree/order 2–60). Values are given in centimetres equivalent water height (cm EWH).

Region	Mean	Median	Std. dev.	Min	Max
Greenland	21.394	19.400	8.046	11.186	88.646
Antarctica	16.564	14.278	9.076	11.052	95.596

References

B. D. Tapley, S. Bettadpur, M. Watkins, and C. Reigber. The gravity recovery and climate experiment: Mission overview and early results. *Geophysical Research Letters*, 31(9), 2004. doi:https://doi.org/10.1029/2004GL019920.

Felix W. Landerer, Frank M. Flechtner, Himanshu Save, Frank H. Webb, Tamara Bandikova, William I. Bertiger, Srinivas V. Bettadpur, Sung Hun Byun, Christoph Dahle, Henryk Dobslaw, Eugene Fahnestock, Nate Harvey, Zhigui Kang, Gerhard L. H. Kruizinga, Bryant D. Loomis, Christopher McCullough, Michael Murböck, Peter Nagel, Meegyeong Paik, Nadege Pie, Steve Poole, Dmitry Strekalov, Mark E. Tamisiea, Furun Wang, Michael M. Watkins, Hui-Ying Wen, David N. Wiese, and Dah-Ning Yuan. Extending the global mass change data record: Grace follow-on instrument and science data performance. *Geophysical Research Letters*, 47(12):e2020GL088306, 2020. doi:https://doi.org/10.1029/2020GL088306.

Kelley Case, Gerhard Kruizinga, and Sien-Chong Wu. GRACE Level 1B Data Product User Handbook, 2010. URL `https://podaac-tools.jpl.nasa.gov/drive/files/allData/grace/docs/Handbook_1B_v1.3.pdf`.

C. Dahle, E. Boergens, I. Sasgen, T. Döhne, S. Reißland, H. Dobslaw, V. Klemann, M. Murböck, R. König, R. Dill, M. Sips, U. Sylla, A. Groh, M. Horwath, and F. Flechtner. Gravis: mass anomaly products from satellite gravimetry. *Earth System Science Data*, 17(2):611–631, 2025. doi:10.5194/essd-17-611-2025. URL `https://essd.copernicus.org/articles/17/611/2025/`.

S. Swenson, D. Chambers, and J. Wahr. Estimating geocenter variations from a combination of grace and ocean model output. *Journal of Geophysical Research*, 113(B08S10), 2008. doi:10.1029/2007JB005338.

B. D. Loomis and K. E. Rachlin. NASA GSFC SLR C20 and C30 solutions (TN-14), Version 3. Online dataset; NASA GSFC SLR Time-Variable Gravity project, 2023. URL `https://earth.gsfc.nasa.gov/sites/default/files/geo/data/slr/tn-14_c30_c20_gsfc_slr.txt`. SLR-derived C_{20} and C_{30} values for GRACE/GRACE-FO gravity field replacement. Data span 4 Apr 2002–1 Sep 2025.

Henryk Dobslaw, Robert Dill, and Christoph Dahle. Grace geopotential gac coefficients gfz rl06, 2018.

I. Velicogna, T. C. Sutterley, and M. R. van den Broeke. Regional acceleration in ice mass loss from greenland and antarctica using grace time-variable gravity data. *Geophysical Research Letters*, 41(22):8130–8137, 2014. doi:https://doi.org/10.1002/2014GL061052.

A Blazquez, B Meyssignac, JM Lemoine, E Berthier, A Ribes, and A Cazenave. Exploring the uncertainty in grace estimates of the mass redistributions at the earth surface: implications for the global water and sea level budgets. *Geophysical Journal International*, 215(1):415–430, 07 2018. ISSN 0956-540X. doi:10.1093/gji/ggy293.

F. Yang, M. Schumacher, L. Retegui-Schiettekatte, A. I. J. M. van Dijk, and E. Forootan. PyGLDA: a fine-scale python-based global land data assimilation system for integrating satellite gravity data into hydrological models. *Geoscientific Model Development*, 18(18):6195–6217, 2025. doi:10.5194/gmd-18-6195-2025.

Wen-Ying Wu, Zong-Liang Yang, Long Zhao, and Peirong Lin. The impact of multi-sensor land data assimilation on river discharge estimation. *Remote Sensing of Environment*, 279:113138, 2022. ISSN 0034-4257. doi:https://doi.org/10.1016/j.rse.2022.113138.

Leire Retegui-Schiettekatte, Maike Schumacher, Henrik Madsen, and Ehsan Forootan. Assessing daily grace data assimilation during flood events of the brahmaputra river basin. *Science of The Total Environment*, 975:179181, 2025. ISSN 0048-9697. doi:https://doi.org/10.1016/j.scitotenv.2025.179181.

Lin Zhang, Yunzhong Shen, Kunpu Ji, and Qiujie Chen. Covariance matrix reconstruction of grace monthly solutions using common factors and individual formal errors. *IEEE Journal of Selected Topics in Applied Earth Observations and Remote Sensing*, 17:15567–15582, 2024. doi:10.1109/JSTARS.2024.3405560.

Eva Boergens. Python package regional tws uncertainty, 2021.

Eva Boergens, Andreas Kvas, Annette Eicker, Henryk Dobslaw, Lennart Schawohl, Christoph Dahle, Michael Murböck, and Frank Flechtner. Uncertainties of GRACE-Based Terrestrial Water Storage Anomalies for Arbitrary Averaging Regions. *Journal of Geophysical Research: Solid Earth*, 127(2):e2021JB022081, 2022. doi:https://doi.org/10.1029/2021JB022081.

A. Güntner, E. Sharifi, J. Haas, E. Boergens, C. Dahle, H. Dobslaw, W. Dorigo, I. Dussailant, F. Flechtner, A. Jäggi, M. Kosmale, K. Luojus, T. Mayer-Gürr, U. Meyer, W. Preimesberger, C. Ruz Vargas, and M. Zemp. Global Gravity-based Groundwater Product (G3P) (Version 1.12). GFZ Data Services, 2024.

Jianli Chen, Byron Tapley, Mark E. Tamisiea, Himanshu Save, Clark Wilson, Srinivas Bettadpur, and Ki-Weon Seo. Error assessment of grace and grace follow-on mass change. *Journal of Geophysical Research: Solid Earth*, 126(9): e2021JB022124, 2021. doi:https://doi.org/10.1029/2021JB022124.

Shengjun Gao, Weifeng Hao, Yi Fan, Fei Li, and Jing Wang. A multi-source grace fusion solution via uncertainty quantification of grace-derived terrestrial water storage (tws) change. *Journal of Geophysical Research: Solid Earth*, 128(11):e2023JB026908, 2023. doi:https://doi.org/10.1029/2023JB026908.

W. You, K. Qian, X. Wan, B. Yu, J. Zhang, L. Pu, J. Shu, and C. Liu. Spatial-domain combination of grace monthly time-variable gravity models based on multiple weighting strategies and comparison of models' performance in the caspian sea. *Scientific Reports*, 15(1):3962, 2025. doi:10.1038/s41598-025-87922-8.

W. R. Peltier, D. F. Argus, and R. Drummond. Comment on "an assessment of the ice-6g_c (vm5a) glacial isostatic adjustment model" by purcell et al. *Journal of Geophysical Research: Solid Earth*, 123:2019–2018, 2018. doi:10.1002/2016JB013844.

Meike Bagge, Volker Klemann, Robert Dill, and Henryk Dobslaw. Present-day gravity changes induced by glacial isostatic adjustment from ensemble simulations with 3d earth structures, 2023.

L. Caron, E. R. Ivins, E. Larour, S. Adhikari, J. Nilsson, and G. Blewitt. Gia model statistics for grace hydrology, cryosphere, and ocean science. *Geophysical Research Letters*, 45(5):2203–2212, 2018. doi:https://doi.org/10.1002/2017GL076644.

Annette Eicker, Lennart Schawohl, Klara Middendorf, Meike Bagge, Laura Jensen, and Henryk Dobslaw. Influence of gia uncertainty on climate model evaluation with grace/grace-fo satellite gravimetry data. *Journal of Geophysical Research: Solid Earth*, 129(5):e2023JB027769, 2024. doi:https://doi.org/10.1029/2023JB027769.

Andreas Groh and Martin Horwath. Antarctic ice mass change products from grace/grace-fo using tailored sensitivity kernels. *Remote Sensing*, 13(9), 2021. ISSN 2072-4292. doi:10.3390/rs13091736.

M. Ablain, B. Meyssignac, L. Zawadzki, R. Jugier, A. Ribes, G. Spada, J. Benveniste, A. Cazenave, and N. Picot. Uncertainty in satellite estimates of global mean sea-level changes, trend and acceleration. *Earth System Science Data*, 11(3):1189–1202, 2019. doi:10.5194/essd-11-1189-2019.

H. Dobslaw, I. Bergmann-Wolf, R. Dill, L. Poropat, M. Thomas, C. Dahle, S. Esselborn, R. König, and F. Flechtner. A new high-resolution model of non-tidal atmosphere and ocean mass variability for de-aliasing of satellite gravity observations: Aod1b rl06. *Geophysical Journal International*, 211(1):263–269, 07 2017. ISSN 0956-540X. doi:10.1093/gji/ggx302. URL `https://doi.org/10.1093/gji/ggx302`.

L. Shihora, Z. Liu, K. Balidakis, et al. Accounting for residual errors in atmosphere–ocean background models applied in satellite gravimetry. *Journal of Geodesy*, 98:27, 2024. doi:10.1007/s00190-024-01832-7. URL `https://doi.org/10.1007/s00190-024-01832-7`.

Andreas Kvas and Torsten Mayer-Gürr. Grace gravity field recovery with background model uncertainties. *Journal of Geodesy*, 93(12):2543–2552, 2019. doi:10.1007/s00190-019-01314-1.

Hao Zhou, Lijun Zheng, Roland Pail, Shuhao Liu, Tiantian Qing, Fan Yang, Xiang Guo, and Zhicai Luo. The impacts of reducing atmospheric and oceanic de-aliasing model error on temporal gravity field model determination. *Geophysical Journal International*, 234(1):210–227, 02 2023. doi:10.1093/gji/ggad064.

S. Bettadpur. *Gravity Recovery and Climate Experiment Level-2 Gravity Field Product User Handbook*. Center for Space Research, The University of Texas at Austin, 2018a. URL `https://archive.podaac.earthdata.nasa.gov/podaac-ops-cumulus-docs/grace/open/docs/L2-UserHandbook_v4.0.pdf`.

E Sinem Ince, Franz Barthelmes, Sven Reißland, Kirsten Elger, Christoph Förste, Frank Flechtner, and Harald Schuh. ICGEM – 15 years of successful collection and distribution of global gravitational models, associated services, and future plans. *Earth Syst. Sci. Data*, 11(2):647–674, May 2019. doi:10.5194/essd-11-647-2019.

Adrian Jäggi, Ulrich Meyer, Martin Lasser, Barbara Jenny, Teodolina Lopez, Frank Flechtner, Christoph Dahle, Christoph Förste, Torsten Mayer-Gürr, Andreas Kvas, Jean-Michel Lemoine, Stéphane Bourgogne, Matthias Weigelt, and Andreas Groh. International combination service for time-variable gravity fields (cost-g). In Jeffrey T. Freymueller and Laura Sánchez, editors, *Beyond 100: The Next Century in Geodesy*, pages 57–65, Cham, 2022. Springer International Publishing. ISBN 978-3-031-09857-4.

Torsten Mayer-Gürr, Saniya Behzadpur, Matthias Ellmer, Andreas Kvas, Beate Klinger, Sebastian Strasser, and Norbert Zehentner. ITSG-Grace2018 - monthly, daily and static gravity field solutions from GRACE, 2018.

Srinivas Bettadpur. Gravity recovery and climate experiment: Utcsr level-2 processing standards document (revision 5.0, april 18, 2018) for level-2 product release 0006. Technical report, Center for Space Research, The University of Texas at Austin, 2018b. URL https://icgem.gfz-potsdam.de/docs/GRACE_CSR_L2_Processing_Standards_Document_for_RL06.pdf. UTCSR Document, Rev 5.0.

Dah-Ning Yuan. Gravity Recovery and Climate Experiment: JPL Level-2 Processing Standards Document for Level-2 Product Release 06. Technical report, Jet Propulsion Laboratory, California Institute of Technology, 2018. URL https://icgem.gfz-potsdam.de/docs/GRACE_JPL_L2_Processing_Standards_Document_for_RL06.pdf. JPL 327-744 (v 6.0).

Christoph Dahle, Michael Murböck, Frank Flechtner, Henryk Dobslaw, Grzegorz Michalak, Karl Hans Neumayer, Oleh Abrykosov, Anton Reinhold, Rolf König, Roman Sulzbach, and Christoph Förste. The GFZ GRACE RL06 Monthly Gravity Field Time Series: Processing Details and Quality Assessment. *Remote Sensing*, 11(18), 2019. ISSN 2072-4292. doi:10.3390/rs11182116.

H. Zhou, L. Zheng, Y. Li, X. Guo, Z. Zhou, and Z. Luo. HUST-Grace2024: a new GRACE-only gravity field time series based on more than 20 years of satellite geodesy data and a hybrid processing chain. *Earth System Science Data*, 16(7):3261–3281, 2024. doi:10.5194/essd-16-3261-2024.

Ingo Koch, Marius Duwe, Jakob Flury, and Ali Shabanloui. Earth's Time-Variable Gravity from GRACE Follow-On K-Band Range-Rates and Pseudo-Observed Orbits. *Remote Sensing*, 13(9):1766, 2021. doi:10.3390/rs13091766.

J.-M. Lemoine and S. Bourgogne. RL05 monthly and 10-day gravity field solutions from CNES/GRGS. In *GSTM2020-51*, 10 2020. doi:https://doi.org/10.5194/gstm2020-51.

Neda Darbeheshti, Martin Lasser, Ulrich Meyer, Daniel Arnold, and Adrian Jäggi. AIUB-G3P GRACE monthly gravity field solutions, 2023.

Martin Lasser, Ulrich Meyer, Daniel Arnold, and Adrian Jäggi. AIUB-GRACE-FO-operational: Operational GRACE Follow-On monthly gravity field solutions - release 02, 2023. URL https://doi.org/10.5880/icgem.2023.004.

Qiujie Chen, Z. Shen, Yunzhong Sun, C. Wu, and Xingfu Zhang. Tongji-GRACE2022: New global temporal earth's gravity field models derived from K-band and LRI inter-satellite range-rate data. In *XXVIII General Assembly of the International Union of Geodesy and Geophysics (IUGG)*, Berlin, Germany, 2023. doi:10.57757/IUGG23-0878.

Franz Barthelmes. Low pass filtering of gravity field models by gently cutting the spherical harmonic coefficients of higher degrees. https://icgem.gfz-potsdam.de/docs/gentlecut_engl.pdf. Accessed 17 December 2025.

J. Ries, S. Bettadpur, R. Eanes, Z. Kang, U. Ko, C. McCullough, P. Nagel, N. Pie, S. Poole, T. Richter, H. Save, and B. Tapley. The combination global gravity model GGM05C. https://hdl.handle.net/2152/74341, 2016.

Khosro Ghobadi-Far, Shin Chan Han, Christopher M. McCullough, David N. Wiese, Richard D. Ray, Jeanne Sauber, Linus Shihora, and Henryk Dobslaw. Along-orbit analysis of GRACE Follow-On inter-satellite Laser Ranging Measurements for sub-monthly surface mass variations. *Journal of Geophysical Research: Solid Earth*, 127, 2 2022. ISSN 2169-9356. doi:10.1029/2021JB022983.

Jorg Kusche, Rainer Schmidt, Sasa Petrovic, and Roelof Rietbroek. Decorrelated GRACE time-variable gravity solutions by GFZ, and their validation using a hydrological model. *Journal of Geodesy*, 83:903–913, 2009. doi:10.1007/s00190-009-0308-3.

Bryant D. Loomis, Kenneth E. Rachlin, David N. Wiese, Felix W. Landerer, and Scott B. Luthcke. Replacing GRACE/GRACE-FO C30 With Satellite Laser Ranging: Impacts on Antarctic Ice Sheet Mass Change. *Geophysical Research Letters*, 47(3):e2019GL085488, 2020. doi:10.1029/2019GL085488.

Pavel Ditmar. Conversion of time-varying stokes coefficients into mass anomalies at the earth's surface considering the earth's oblateness. *Journal of Geodesy*, 92:1401–1412, 2018. doi:10.1007/s00190-018-1128-0.

Igor Koch, Mathias Duwe, and Jakob Flury. Residual and unmodeled ocean tide signal from 20+ years of grace and grace-fo global gravity field models. *Journal of Geophysical Research: Solid Earth*, 129(9):e2024JB029345, 2024. doi:https://doi.org/10.1029/2024JB029345.

Nijia Qian, Guobin Chang, Pavel Ditmar, Jingxiang Gao, and Zhengqiang Wei. Sparse ddk: A data-driven decorrelation filter for grace level-2 products. *Remote Sensing*, 14(12), 2022. ISSN 2072-4292. doi:10.3390/rs14122810.

Loren Carrère, F Lyard, M Cancet, A Guillot, N Picot, et al. Fes 2014, a new tidal model—validation results and perspectives for improvements. In *Proceedings of the ESA living planet symposium*, pages 9–13, 2016.

R. D. Ray. Precise comparisons of bottom-pressure and altimetric ocean tides. *Journal of Geophysical Research: Oceans*, 118(9):4570–4584, 2013. doi:https://doi.org/10.1002/jgrc.20336.

F. H. Lyard, D. J. Allain, M. Cancet, L. Carrère, and N. Picot. FES2014 global ocean tide atlas: design and performance. *Ocean Science*, 17(3):615–649, 2021. doi:10.5194/os-17-615-2021.

Roman Savcenko and Wolfgang Bosch. EOT11a-empirical ocean tide model from multi-mission satellite altimetry. Technical report, Deutsches Geodätisches Forschungsinstitut (DGFI), 2012.

F. Lyard, F. Lefevre, T. Letellier, and O. Francis. Modelling the global ocean tides: modern insights from FES2004. *Ocean Dynamics*, 56:394–415, 2006. doi:10.1007/s10236-006-0086-x.

Henryk Dobslaw, Robert Dill, Meike Bagge, Volker Klemann, Eva Boergens, Maik Thomas, Christoph Dahle, and Frank Flechtner. Gravitationally consistent mean barystatic sea level rise from leakage-corrected monthly grace data. *Journal of Geophysical Research: Solid Earth*, 125(11):e2020JB020923, 2020. doi:https://doi.org/10.1029/2020JB020923. URL `https://agupubs.onlinelibrary.wiley.com/doi/abs/10.1029/2020JB020923`. e2020JB020923 10.1029/2020JB020923.

S. Werth, A. Güntner, R. Schmidt, and J. Kusche. Evaluation of GRACE filter tools from a hydrological perspective. *Geophysical Journal International*, 179(3):1499–1515, 12 2009. ISSN 0956-540X. doi:10.1111/j.1365-246X.2009.04355.x.

Denis L. Volkov and Lee-Lueng Fu. The role of vorticity fluxes in the dynamics of the Zapiola Anticyclone. *Journal of Geophysical Research: Oceans*, 113(C11), 2008. doi:https://doi.org/10.1029/2008JC004841. URL `https://agupubs.onlinelibrary.wiley.com/doi/abs/10.1029/2008JC004841`.

Y. Yu, B. F. Chao, D. García-García, and Z. Luo. Variations of the Argentine Gyre observed in the GRACE time-variable gravity and ocean altimetry measurements. *Journal of Geophysical Research: Oceans*, 123(8):5375–5387, 2018. doi:https://doi.org/10.1029/2018JC014189. URL `https://agupubs.onlinelibrary.wiley.com/doi/abs/10.1029/2018JC014189`.

M. Cuadrat-Grzybowski, J. G. Teixeira da Encarnacao, and P. N. A. M. Visser. Potential of Ka-Band Range Rate Post-Fit Residuals for High-Frequency Mass Change Applications. *Journal of Geophysical Research: Solid Earth*, 130(12), 2025. doi:https://doi.org/10.1029/2025JB031615.

R. D. Ray and S. B. Luthcke. Tide model errors and GRACE gravimetry: towards a more realistic assessment. *Geophysical Journal International*, 167(3):1055–1059, 12 2006. ISSN 0956-540X. doi:10.1111/j.1365-246X.2006.03229.x.

Wei Liu and Nico Sneeuw. Aliasing of ocean tides in satellite gravimetry: a two-step mechanism. *Journal of Geodesy*, 95:134, 2021. doi:10.1007/s00190-021-01586-6.

Zhen Li, Zizhan Zhang, and Hansheng Wang. On Tide Aliasing in GRACE Time-Variable Gravity Observations. *Remote Sensing*, 14(21), 2022. ISSN 2072-4292. doi:10.3390/rs14215403.

S.-C. Han, R. Ray, and C. Hughes. High-frequency (20–60 days) ocean mass variation over the Argentine Basin observed from GRACE. In *Proceedings of the GRACE Science Team Meeting*, 2014. URL `https://www.gfz-potsdam.de/en/section/global-geomonitoring-and-gravity-field/projects/gravity-recovery-and-climate-experiment-follow-on-grace-fo-mission/gstm/gstm-2014/`.